CHALMERS
UNIVERSITY OF TECHNOLOGY

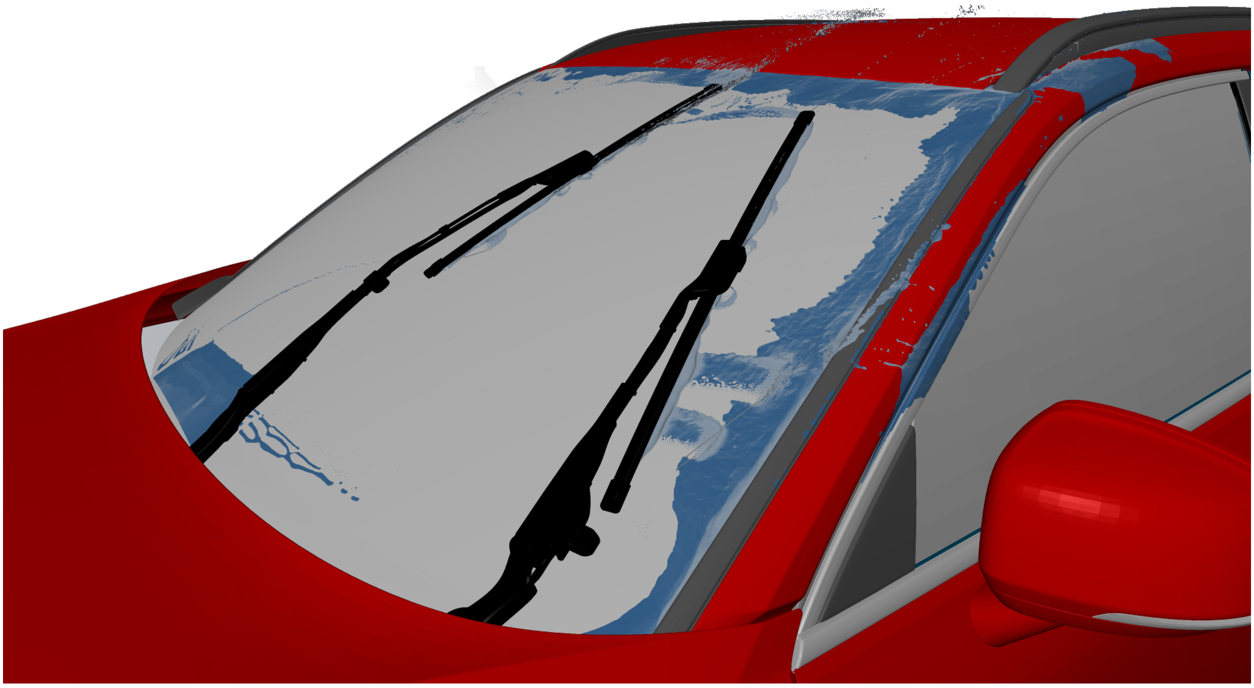

Modelling A-pillar Overflow - Using a Smoothed Particle Hydrodynamics Based Method

Master's thesis report in Applied Mechanics

MARTIN LARSSON

DEPARTMENT OF MECHANICS AND MARITIME SCIENCES
CHALMERS UNIVERSITY OF TECHNOLOGY
Gothenburg, Sweden 2022
www.chalmers.se

Master's thesis report 2022

Modelling A-pillar Overflow - Using a Smoothed Particle Hydrodynamics Based Method

MARTIN LARSSON

CHALMERS
UNIVERSITY OF TECHNOLOGY

Department of Mechanics and Maritime Sciences
Division of Fluid mechanics
Chalmers University of Technology
Gothenburg, Sweden 2022

Modelling A-pillar Overflow - Using a Smoothed Particle Hydrodynamics Based Method
Martin LARSSON

Supervisor: Lu Naixian, Volvo Cars
Examiner: Srdjan Sasic, Department of Mechanics and Maritime Sciences

Master's Thesis report 2022
Department of Mechanics and Maritime Sciences
Division of Fluid mechanics
Chalmers University of Technology
SE-412 96 Gothenburg
Telephone +46 31 772 1000

Cover: Volvo XC40 wiper simulation in PreonLab

Typeset in LaTeX
Printed by Chalmers Reproservice
Gothenburg, Sweden 2022

Modelling A-pillar Overflow - Using a Smoothed Particle Hydrodynamics Based Method
MARTIN LARSSON
Department of Mechanics and Maritime Sciences
Chalmers University of Technology

Abstract

A-pillar overflow is the event when fluid is transported from the windshield across the A-pillar, ending up on the driver side window, obscuring the driver's vision. Simulations of A-pillar overflow can make initial predictions of how the driver's vision will be affected during windscreen washing or rain, and reduce developmental costs by making earlier design changes.

Earlier numerical simulations have been carried out using traditional Finite Volume Method (FVM) Computational Fluid Dynamics-solvers (CFD) based on hybrid methods using Lagrangian Particle Tracking (LPT) and Volume of Fluid (VOF). Since A-pillar overflow is a transient event with moving wipers, requiring a transient mesh, it increases the computational cost and can induce numerical instabilities. By applying a Smoothed Particle Hydrodynamics (SPH) solver the need for a mesh is removed, but this approach has less validated solvers and problems with particle size-dependent model constants. This thesis aims at investigating A-pillar overflow using an SPH-based solver, PreonLab, and qualitatively validate the simulation with physical tests.

The purpose of the thesis is firstly to establish a feasible workflow to simulate a windscreen washing event. The wiper kinematics modelled by a multibody dynamics software, ADAMS, and the airflow computed by an FVM method in Star-CCM+ are imported to PreonLab. Model constants such as particle spacing, adhesion and roughness factor are studied using validation against simple physical test cases. Secondly, it is to simulate A-pillar overflow on the Volvo V90 and XC40, where the amount of liquid arriving on the driver side window is substantially different due to different styling around the A-pillar area.

Results indicate that wiper cycle simulations could be conducted in PreonLab in the future, as the overall behaviour of the fluid is captured through tuning of model parameters. Due to a lack of validation of the surface parameters and the density used in the airflow implementation, the simulation method is not fully validated. Further studies on airflow-liquid interaction models and surface properties need to be done in order to capture the complicated physics of an A-pillar overflow simulation.

Keywords: Wipers, Smoothed-Particle Hydrodynamics, IISPH, A-pillar overflow, Computational Fluid Dynamics, Surface wetting, Pairwise Force model.

Acknowledgements

This thesis was conducted at the Contamination & Core CFD group at Volvo Cars and I would like to thank my supervisor Dr. Lu Naixian (Senior CAE Engineer) for all the discussions, patience and support when I needed throughout the thesis. I would also like to thank Dr. Torbjörn Virdung (Technical Expert) who helped initiate this thesis. A warm thank you to everyone at the Contamination & Core CFD group for the discussions in the lunch room and for letting me be a part of the group, making the time of my thesis truly enjoyable.

I would also like to thank my examiner Professor Srdjan Sasic at Chalmers for the discussions and time. A big thanks to both Fifty2 and MSC Software for their support, without their help it would have been much harder.

Lastly, I would like to thank my family and friends for their support during my years at Chalmers.

Martin Larsson, Gothenburg, June 2022

Nomenclature

Abbreviations

APM	A-Pillar Moulding
CFD	Computational Fluid Dynamics
CSF	Continuum Surface Force
DS	Driver Side
$ECTS$	European Credit Transfer System
EOS	Equation Of State
FVM	Finite Volume Method
GUI	Graphical User Interface
$IISPH$	Implicit Incompressible Smoothed Particle Hydrodynamics
OEM	Original Equipment Manufacturer
$PCISPH$	Predictor-Corrector Incompressible Smoothed Particle Hydrodynamics
PF	Pairwise Force
PPE	Pressure Poisson Equation
PS	Passenger Side
SPH	Smoothed Particle Hydrodynamics
$SSPH$	Standard Smoothed Particle Hydrodynamics
SUV	Sport Utility Vehicle
UV	Ultraviolet
VOF	Volume Of Fluid
$WCSPH$	Weakly Compressible Smoothed Particle Hydrodynamics

Symbols

δ	Dirac delta function
η	Constant to avoid infinity
γ	Surface energy
$\boldsymbol{\nabla}$	Gradient
κ	Surface curvature
μ	Dynamic viscosity

ϕ	Surface tension force
ρ	Density
σ	Surface tension
$\mathbf{f}$	Body force
$\mathbf{n}$	Surface normal
$\mathbf{V}$	Velocity
θ	Contact angle
A_p	Projection area
C_d	Coefficient of drag
d	Ratio of particle diameter and distance from particle center
F_d	Drag force
h	Cut-off length
p	Pressure
r	distance from particle center
$t*$	Unit less time
W	Kernel function
W_{ii}	Work of adhesion between surface i and surface i

Contents

List of Figures

List of Tables

1

Introduction

A-pillar overflow describes the event of fluid from the windscreen moving over the A-pillar and onto the side screen. Specifically, A-pillar overflow from a windscreen cleaning event is investigated in this thesis. The ability to predict and model this event is of interest since fluid on the side screen affects the driver's side- and rearwards visibility. A realistic numerical model of A-pillar overflow is a good tool to enhance safety and lower developmental costs as design changes can be tested in a quicker and cheaper way.

1.1 Background

Regardless of the type of A-pillar overflow, it is a cause for an impaired vision for the driver and in turn a safety concern. Due to the design of a traditional wiper system with the wiper shafts located toward the driver side most of the A-pillar overflow will occur on the driver side, leaving the passenger side with a better capability of dispersing the potential overflow to the roof of the vehicle. How the front part of a vehicle is designed is the result of several different aspects weighed against each other and will affect the amount of A-pillar overflow. The problem is not designing a vehicle with low amounts of A-pillar overflow, but designing a vehicle which strikes a balance between factors such as design, aerodynamics, aeroacoustics and the vehicle's ability to handle a crash. Aspects that affect A-pillar overflow include, but are not limited to, A-pillar slanting angle, design of A-pillar mouldings (APM), windscreen curvature, layout and design of the windscreen cleaning system. Potential implications of large APM are aerodynamic drag, induced cabinet noise and less visually appealing design. On the other hand, with no APM it is much harder to minimize A-pillar overflow since the water or washing liquid is more likely to go over the A-pillar and end up on the front side window. Since these are components that are vital to many areas of development it is important to have the ability to predict A-pillar overflow during the early stages of development. An overview of the important parts that affect the A-pillar overflow can be seen in Figure 1.1.

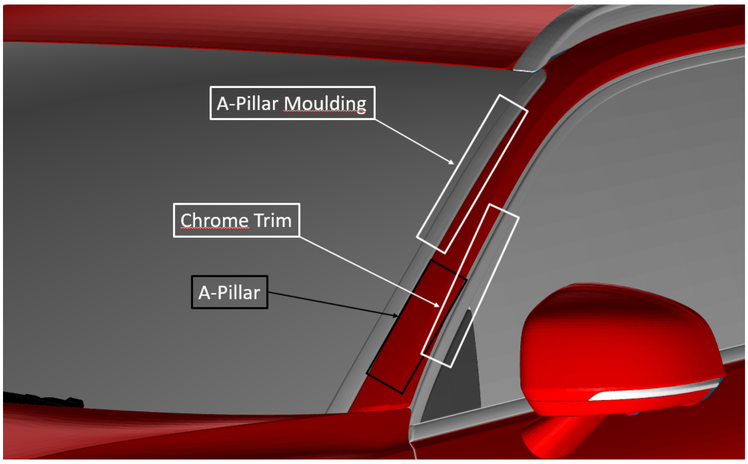

Figure 1.1: Overview of the A-pillar area of a Volvo XC40

There are many challenges of modelling overflow where the most prominent factors are airflow interaction, the action of the wipers, injection of liquid into the domain and surface interaction of different materials with the liquid. The majority of these factors are supported through other departments at Volvo Cars. In other words, the modelling of A-pillar overflow is a cross-disciplinary subject.

The current method for computing A-pillar overflow from windscreen cleaning is using the current industry standard of Computational Fluid Dynamics (CFD), Finite Volume Method (FVM) based solvers (Star-CCM+, Fluent, OpenFOAM etc) using hybrid methods with Lagrangian Particle Tracking (LPT), Eulerian Wall Film (EWF) and Volume of Fluid (VOF). In short, with the current method, particles are injected as Lagrangian particles where they then impinge on the surface and when doing so, become an Eulerian Wall Film (EWF). When the fluid film reaches a certain thickness it is transferred to a Volume of Fluid (VOF) model. There are three different methods utilised with an interaction step between each of them, creating not only a complex but a computationally heavy simulation setup, especially when combined with a moving wiper system. The method is also prone to diverging mainly due to the limitations of handling a time-dependent mesh. There are also simpler setups used, each with its own limitations.

The Smoothed-Particle Hydrodynamics (SPH) solvers have gained popularity in the last few years as it is a Lagrangian meshfree method, and will not carry the same disadvantages as the FVM-based solvers in terms of mesh and stability issues. In the SPH-based solvers everything is modelled using particles with several properties such as size, velocity, mass, surface models etc. Some drawbacks of the SPH-based solvers are the same as those of the traditional FVM-based solvers. For example to fully capture the events of a turbulent aerodynamic flow an almost infinite amount of particles would be needed even for small cases (approaching the Direct Numerical Solution in both accuracy and computational cost). For fluids with higher viscosity (water, paint etc) the SPH-based solvers seem to capture the physics well.

1.2 Problem Statement

1.2.1 Aim & Objectives

The aim of the thesis can be split into two parts, with the first aim being the development of an SPH-based simulation model to see if it can be a replacement for an FVM-based simulation model.

The second aim is to use the derived simulation model and apply it to two vehicle models, Volvo V90 and Volvo XC40, which have substantially different amounts of A-pillar overflow. Reason being that if the simulation model can predict overflow accurately for both vehicle models it should be able to predict overflow for vehicle models with similar amounts of A-pillar overflow.

1.2.2 Delimitations

The main delimitations of the thesis can be listed as,

- Limited to 60 ECTS for one student.
- CAD models available are that of the production vehicles and the various tests concerning A-pillar overflow are from the later stages of development.
- Lack of information regarding surface properties around the A-pillar area, including the windscreen, A-pillar moulding, painted steel, painted aluminium, and rubber in wiper blades.

The software used throughout the thesis and the version is,

- PreonLab, Version: 5.1.1 and 5.2.0a (alpha)
- ADAMS, Version: 2019.2
- ANSA, Version: 20.1.4
- CATIA, Version: V5R6-2016

1.3 Structure of the Report

The report is divided into the following chapters: *Introduction*, *Theory*, *Methods*, *Results & Discussion* and *Conclusion*.

The *Introduction* aims at providing the reader with a general background of how A-pillar overflow has traditionally been modelled, why an SPH-based simulation model could be beneficial and what the drawbacks are. The chapter also describes the purpose of the thesis and the outline of the report.

The *Theory*, see Chapter 2, explains how a generic SPH-based solver works and the equations behind it. The kernel function and surface tension forces are explained in closer detail due to their higher importance to the thesis and SPH-based solvers.

The *Method*, see Chapter 3, explains the vehicle models used and which physical validation tests were carried out and how. The wiper movement modelling and airflow modelling are explained as well as the A-pillar overflow simulation setup.

Results & Discussion, see Chapter 4, covers the results and discussion from the physical validation tests and the A-pillar overflow simulation results. *Results & Discussion* combines both results and discussion to ease the readability of the report.

The *Conclusion*, see Chapter 5, provides the reader with a summary of the results and how it relates to the purpose. It also covers the suggested future work to continue to improve A-pillar overflow simulations, or simulations where surface-liquid interaction is of great importance.

2

Theory

The framework and equations used in a generic SPH solver are presented and explained in this chapter. The two different frameworks used in CFD depending on if the solver is SPH-based or FVM-based is covered. More focus will be put on surface tension forces as these are of higher importance for this thesis.

2.1 Eulerian and Lagrangian Framework

There are two frameworks used when modelling fluid; one is when the viewer is observing how fluid changes within certain locations of a flow and one is when the viewer is following a certain partition of fluid. The first way is called the Eulerian framework and the latter is called the Lagrangian framework. A traditional way of analysing the fluid in an Eulerian framework is by dividing an area, or volume, into finite cells and looking at the fluid particles entering or leaving the cell. The Lagrangian framework on the other hand doesn't divide the volume into cells, but instead divides the fluid into smaller partitions and follows them individually. The main framework used in this thesis is the Lagrangian framework. Figure 2.1 shows an example of both Eulerian and Lagrangian frameworks,

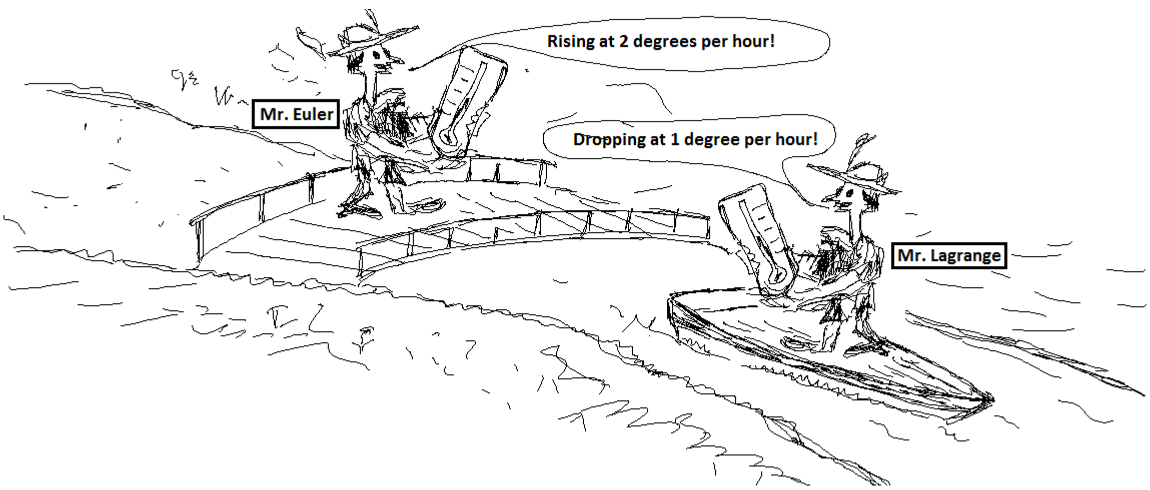

Figure 2.1: Difference between Eulerian and Lagrangian framework, Mr Eulerian is standing on the bridge and Mr Lagrangian is going with the flow in his boat. *Source: https://www.flowillustrator.com/*

2.2 Navier-Stokes Equation and the Smoothed Particle Hydrodynamics Implementation

The first applications of Smoothed Particle Hydrodynamics (SPH) emerged during the late 70's as a way of modelling nonaxisymmetric phenomenas in astrophysics [1]. It was later realised that the method could be applied to not only astrophysics, but also to fluid dynamics. A major benefit of SPH, since it uses a Lagrangian framework, is that it does not require a mesh and that it also can be implemented to conserve mass, momentum and energy [2].

Some of the drawbacks are that the commercial SPH software used is quite new in terms of industrial CFD application, despite having research applications since the 70's. The main disadvantage is that these commercial solvers are less validated, they have fewer solver settings and overall less documentation on implementation.

The basis of understanding the SPH solvers and the modelling of fluid dynamics is the understanding of the Navier-Stokes equation. The Navier-Stokes equation contains all information required to model fluids. Since the discretization of the Navier-Stokes and its implementation into the SPH solver is closely coupled, this section serves to provide the basics of the Navier-Stokes from a Lagrangian framework. In this thesis only incompressible flow will be considered, since the solver used in this thesis is based on that assumption, and the Navier-Stokes equation for incompressible flow in a Lagrangian framework reads,

$$\frac{d\mathbf{v}_a}{dt} = -\rho\boldsymbol{\nabla}p_a + \frac{1}{\rho}\boldsymbol{\nabla}(\mu\boldsymbol{\nabla}\mathbf{v}_a) + \mathbf{f}_a + \boldsymbol{\nabla}\phi_a \tag{2.1}$$

$\frac{d\mathbf{v}_a}{dt}$ describes the acceleration of the fluid where $\mathbf{v}_a$ is the velocity vector of particle a. $-\rho\boldsymbol{\nabla}p_a$ describes the pressure force, where ρ is the density of the fluid, $\boldsymbol{\nabla}$ is the differential operator with respect to direction, $\frac{d}{dx_i}+\frac{d}{dx_j}+\frac{d}{dx_k}$, p_a is pressure of particle a. $\frac{1}{\rho}\boldsymbol{\nabla}(\mu\boldsymbol{\nabla}\mathbf{v}_a)$ describes the viscous forces where ρ is the density, μ is the dynamic viscosity. f_a is the body force, examples of body forces are gravity and drag. The last term, $\boldsymbol{\nabla}\phi_a$, represents the surface tension force of particle a. Depending on the literature the surface tension force, ϕ_a, might be grouped together with the body forces, $\mathbf{f}_a$, but in this thesis the surface forces are highly important and a separate chapter is dedicated to how the surface forces are modelled.

2.2.1 Kernel function and its use within Smoothed Particle Hydrodynamics

Applying Equation 2.1 directly to solve a problem would be computationally expensive and inefficient. This is due to the fact that every particle would have to consider every single one of the other particles in the system. Naturally, the larger the distance between two particles, the lower the interaction between them would be. The opposite is also intuitively true, the closer the particles are to each other, the stronger the interaction. The way this is handled is often through the use of a kernel function. This function weighs the impact the particles' scalar fields have on the distance between the observed particle and the other particles in the system. Which kernel formulation to use and its implication on the result is a study on its own, but some examples of kernels are cubic, quadratic, Gaussian and Wendland kernels. An example of a cubic kernel is [1],

$$W = \begin{cases} \frac{1}{\pi h^3}(1 - \frac{3}{2}d^2(1 - \frac{d}{2})) & \text{for } 0 < d < 1 \\ \frac{1}{4\pi h^3}(2 - d)^3 & \text{for } 1 < d < 2 \\ 0 & \text{for } d > 2 \end{cases} \tag{2.2}$$

A visualisation of the cubic kernel function is seen in Figure 2.2,

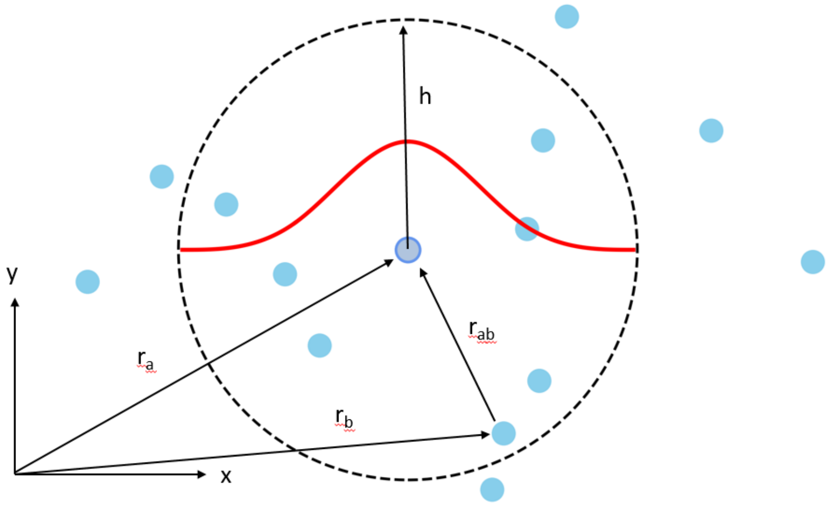

Figure 2.2: Visualisation of a cubic kernel function with the darker blue circle as the particle of reference.

In Figure 2.2 the dotted black circle marks the cut-off length, h. The red line shows the impact on particle a from another particle in the system as a function of the distance r_{ab}. The black lines from origo to particles a and b are the distance vectors from origo to the respective particle.

The impact of the kernel function is better understood by showing its use with an arbitrary scalar field function,

$$f(r) = \int_V f(r')\delta(r - r')dr' \tag{2.3}$$

Where $f(r)$ is any scalar function, δ is the Dirac delta function and r' and r are two positions in space (and in the volume V). The Dirac delta function is derived from the kernel function when a smoothing length, h, is introduced. [3]

$$\lim_{h\to 0} W(r, h) = \delta(r) \tag{2.4}$$

The kernel function has an important property, which is that it is always normalised as,

$$\int_V W(r,h)dr' = 1 \tag{2.5}$$

The smoothing kernel is symmetric, meaning that the order of r and r' has no effect on the kernel value. Using first order Taylor expansion to expand the kernel function using $\delta(r - r', h)$, the scalar function is now [3],

$$f(r) = \int_V f(r')W(r - r', h)dr' + \mathcal{O}(h^2) \tag{2.6}$$

By using a cut-off length the computational cost can be decreased, which is the goal when implementing a kernel function. In Equation 2.2 the cut-off length used was 2.

2.2.2 Pressure forces

The pressure forces in Equation 2.1 can be formulated in several ways, but one of the most common forms in SPH is Equation 2.7, where the kernel function $W_{a,b}$ is used [4].

$$-\rho\boldsymbol{\nabla}p_a = -m_a\sum_{b=1}^{n}(\frac{p_a}{\rho_a^2} + \frac{p_b}{\rho_b^2})\boldsymbol{\nabla}_a W_{a,b} \tag{2.7}$$

In Equation 2.7, a denotes the particle on which the equation is based and b is one of the neighbouring particles ($b = 1, 2, ..., n$) . The mass of the particle is denoted as m.

2.2.3 Viscous forces

The viscous forces in Equation 2.1 are discretized as,

$$\boldsymbol{\nabla}(\mu\boldsymbol{\nabla}\mathbf{V}_a) = \sum_{b=1}^{n} m_b(\mu_a + \mu_b)\frac{1}{\rho_a\rho_b}\mathbf{v}_{a,b}(\frac{1}{|r_{a,b}| + \eta}\frac{\partial W}{\partial r_{a,b}}) \tag{2.8}$$

In Equation 2.8, the constant η is used to avoid infinity as $|r_{a,b}|$ approaches zero. The actual value of the constant depends on the simulation performed but a usual value of η is $0.01d$, where d is the particle diameter [4].

2.2.4 Body forces

The body forces in Equation 2.1 include the gravitational force on the particles as well as the drag forces from the air on the liquid particles. Several approaches can be implemented when including air in the model. One method is to introduce a two-way coupling between the air and the liquid. This is the most realistic, but also the most computationally expensive method. Another option is to simply discard the liquid-gas interaction and only model the liquid, which has the most impact on the result. To discard the forces from the airflow can be an appropriate method for applications where the inertia of the liquid is dominant. Examples of this is the modelling of a dam break or a vehicle wading through water. When the air is exerting a lot of force compared to the inertia of the liquid, such as in this thesis, this is not a valid option. A third option is to introduce a one-way coupling between the airflow and the liquid, which is appropriate if the effect of the liquid on the airflow is not of interest, or of small magnitude. The chosen approach in this thesis dealing with windscreen washing is therefore the third option, using a one-way coupling.

The commercial solver uses the drag equation, see Equation 2.9. The force field is a set of velocity vector values that are interpolated on the particle, which can be seen as f_i in Equation 2.1. The drawback to this approach, as previously mentioned, is that the airflow is not affected by the liquid particles, but since the airflow flow structure on a larger scale is not significantly affected it is a reasonable simplification. The implementation used stems from the drag equation,

$$F_d = \frac{1}{2} C_d \rho A_p V^2 \tag{2.9}$$

Where F_d is the drag force, C_d is the drag coefficient and A_p is the projected area. The velocity implemented is the velocity difference between the fluid particle and the air,

$$V^2 = |V_a - V_i|^2 \frac{V_a - V_i}{|V_a - V_i|} = |V_a - V_i|(V_a - V_i) \tag{2.10}$$

Where V_i is the velocity vector of particle i and V_a is the velocity vector of the air. The implementation features a variable C_d, dependent on the velocity difference $V_i - V_a$. A large velocity difference induces a C_d that corresponds to a disk and a small velocity difference with that of a perfect, rigid sphere. The model implemented is based on the work of Liu [5].

2.2.5 Surface tension forces

Surface and interfacial energies between fluids and solids need to be fully grasped in order to understand how surface tension is modelled in the body force term in the Navier-Stokes equation. If only considering the adhesion of a liquid in vacuum it depends on the energy change as two unit areas of liquid were to separate. This is called the work of adhesion, W_{12}, where 1 and 2 are unit area of liquid 1 and 2 respectively. The surface energy of a liquid in vacuum is the free energy change as the area of the liquid is increased by 1 unit area. This is also the same energy as separating one unit area of liquid into two half-unit areas,

$$\gamma_1 = \frac{1}{2} W_{11} \tag{2.11}$$

The interfacial energy between two different liquids can be calculated by,

$$\gamma_{12} = \frac{1}{2} W_{11} + \frac{1}{2} W_{22} - W_{12} \tag{2.12}$$

The first term, W_{11}, is the surface energy of half a unit area of liquid 1. The second term, W_{22}, is the surface energy between half a unit area of liquid 2, and the last term, W_{12}, is the interfacial energy between one unit area of contact between liquid

1 and 2.

For a solid-liquid interaction it is the same as for Equation 2.12,

$$\gamma_{12} = \frac{1}{2}W_{11} + \frac{1}{2}W_{22} - W_{12} = \gamma_S + \gamma_L - W_{SL} \tag{2.13}$$

The index was changed for clarification with "S" denoting solid and "L" denoting liquid. The most apparent effect is the contact angle between a liquid and a solid. The contact angle is defined as the point where the liquid, solid and gas phase meets, this is called the triple point. The angle is measured from the solid plane underneath the liquid and along the tangential of the surface of the droplet at the triple point, an example of a contact angle measurement is seen in Figure 2.3.

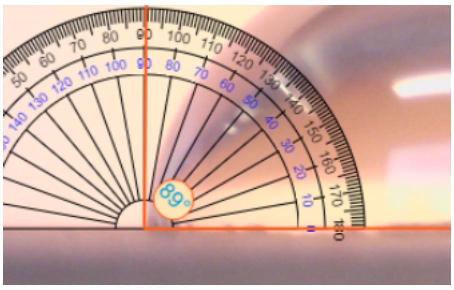

Figure 2.3: Contact angle measurement of a water droplet on rubber trim

The contact angle is a consequence of the total energy of the system and can be described by,

$$W_{tot} = \gamma_{GL}(A_c + A_f) - W_{SGL}A_f \tag{2.14}$$

The area of the liquid in contact with the gas is the area with a curvature and is the A_c term found on the right side and A_f is the flat area in contact with the solid. Assuming that the droplet volume is constant then $\frac{dA_c}{dA_f} = cos(\theta)$ and the following can be derived.

$$\gamma_{SG}(1 + cos(\theta)) = W_{SGL} = \gamma_{SG} + \gamma_{LG} - \gamma_{SL} \tag{2.15}$$

Assuming that the droplet is at equilibrium the Equation 2.16 describes the relationship between the interfacial energies and the contact angles [6],

$$\gamma_{SG} - \gamma_{GL}cos(\theta_0) = \gamma_{SL} \tag{2.16}$$

Equation 2.15 and Equation 2.16 are general forms of the Young-Dupré equation which, if the gas is assumed to be inert, reads.

$$\gamma_L(1 + cos(\theta)) = W_{12} \tag{2.17}$$

A variation of the Equation 2.17 is the Young equation.

$$\gamma_{SL} + \gamma_L cos(\theta) = \gamma_S \tag{2.18}$$

The Young equation stems from Equation 2.16 but with the assumption that the gas is inert. The value of γ_L for water is $0.072N/m$ and the constants γ_{SL} and γ_S

are material specific.

The static contact angle can vary between samples and this phenomena is known as contact angle hysteresis. The largest contact angle is referred to as the advancing contact angle and the lowest is referred to as the receding contact angle. Which contact angle the droplet will have depends on the droplet's history. The dynamic behavior of contact angles is a complex subject and different solutions to modelling it exist in FVM-based solvers. With SPH-based solvers there are no explicit implementations to capture the dynamics of contact lines. When the triple point of a droplet moves, for example when a rivulet moves on a vertical glass window, it introduces a moving contact line and a lot of complexity is added. The different combinations of receding and advancing contact angles are infinite for a moving contact line. Another aspect is how one looks at the contact line, a macroscopic approach focuses on the contact angle visible with the eyes whereas the microscopic contact angle is the one locally closest to the surface. Both the microscopic and macroscopic contact angle is affected by surface contaminants and the study of moving contact lines is a complex study on its own.

The two most common approaches to modelling surface tension are the Continuum Surface Force (CSF) and the Pairwise Force model (PF). The different models have different strengths and weaknesses, which has a profound effect on the fluid modelled. The CSF model applies Young's equation directly,

$$\boldsymbol{\nabla} \cdot p = -\sigma \boldsymbol{\nabla}(\mathbf{n}) \tag{2.19}$$

Where σ is the surface tension between the two particles, i.e γ_{SL}, and $\mathbf{n}$ is the surface normal of the fluid. The implementation in the CSF model reads as follows,

$$\boldsymbol{\nabla} \cdot p = -\sigma \kappa \mathbf{n} \delta \tag{2.20}$$

In Equation 2.20 the curvature of the surface, κ, is taken into account. The CSF model applies a finite volume over the interface region between the different fluids. The main advantage of the CSF model is that it relies on the actual physical values of the surface tension forces. The drawback is that a surface normal always has to be calculated. This is a cumbersome process, especially for coarser particles.

In contrast, the PF model employs a function depending on distance, see Equation 2.21,

$$\boldsymbol{\nabla} \phi_a = -\sum_b \sigma \omega^c(q) \frac{\mathbf{r}_{ab}}{h^2} \tag{2.21}$$

From Equation 2.21 it is clear that the PF model does not use a surface normal, which is one of its great strengths. The q in kernel function, ω^c, is the distance between particle a and b divided by the cut-off length, $q = \frac{\mathbf{r}_{ab}}{h}$. The PF model employs a different kernel function than previously mentioned in 2.2, since the kernel coupled to the PF needs to apply a repelling force if the neighbouring particles get too close. It also serves as a way of reducing computational cost as particles at a distance h do not affect the surface tension force.

2.2.6 Smoothed Particle Hydrodynamics Solver Implementation

The discretization of the Navier-Stokes Equation in the SPH solver has been covered, but the actual implementation has not. There are several ways of implementing it, and the first major question is how to solve pressure-velocity-coupling. Common approaches are:

- *Standard SPH (SSPH):* Pressure-velocity coupling done using an Equation of State (EOS), which has proven to be useful for compressible fluids.
- *Weakly Compressible SPH (WCSPH):* Stiff EOS is used and capable of giving good results but at an expensive computational cost.
- *Predictor-Corrector Incompressible SPH (PCISPH):* Variation of the SSPH-method using different predictor-corrector algorithms to improve time-step length.
- *Implicit Incompressible SPH (IISPH):* The pressure-velocity coupling is done using a discretization of the continuity equation and the Pressure Poisson Equation (PPE).

The SPH solver used in this thesis is based on the last example, Implicit Incompressible SPH (IISPH). In the IISPH method there is an intermediate velocity calculated without considering the pressure forces. Then the velocity is corrected using the PPE and the continuity equation. How the PPE is formulated depends on how it was derived. An example of a PPE is Equation 2.22.[7]

$$\Delta t^2 \sum_j m_j \left(\frac{\mathbf{F}_i^p(t)}{m_i} - \frac{\mathbf{F}_j^p(t)}{m_j}\right) \nabla W_{ij}(t) = \rho_0 - \rho_i^{adv} \tag{2.22}$$

ρ_0 is the rest density, ρ_i^{adv} is the intermediate density. The rest density and the intermediate density make up the right-hand side and the unknown pressure forces, $\mathbf{F}_i^p(t)$ and $\mathbf{F}_j^p(t)$ are solved for. Further explanation of the implementation will not be covered in this thesis but all of the methods of handling the SPH implementation have their advantages and drawbacks.

3
Method

This chapter outlines the geometries and the workflow used. In *Geometry*, see Section 3.1, the two vehicle models used for the A-pillar overflow simulations are presented. An introduction to the SPH software used in the thesis can be found under *PreonLab*, see Section 3.2. Two separate studies were conducted with the aim of capturing the static and dynamic behaviour of droplets in PreonLab. The first study, with the aim of capturing the static contact angles of droplets on different materials, is described in Section 3.3. The second study, with the aim of capturing the dynamic behaviour of droplets impacting a glass surface, is described in Section 3.4. Airflow implementation is covered in Section 3.5 and the wiper kinematics modelling is described in Section 3.6. Section 3.8, *A-Pillar Overflow Simulations*, outlines how the airflow field is implemented as well as which simulations were performed. A flowchart of the workflow used to simulate A-pillar overflow is presented in Figure 3.1.

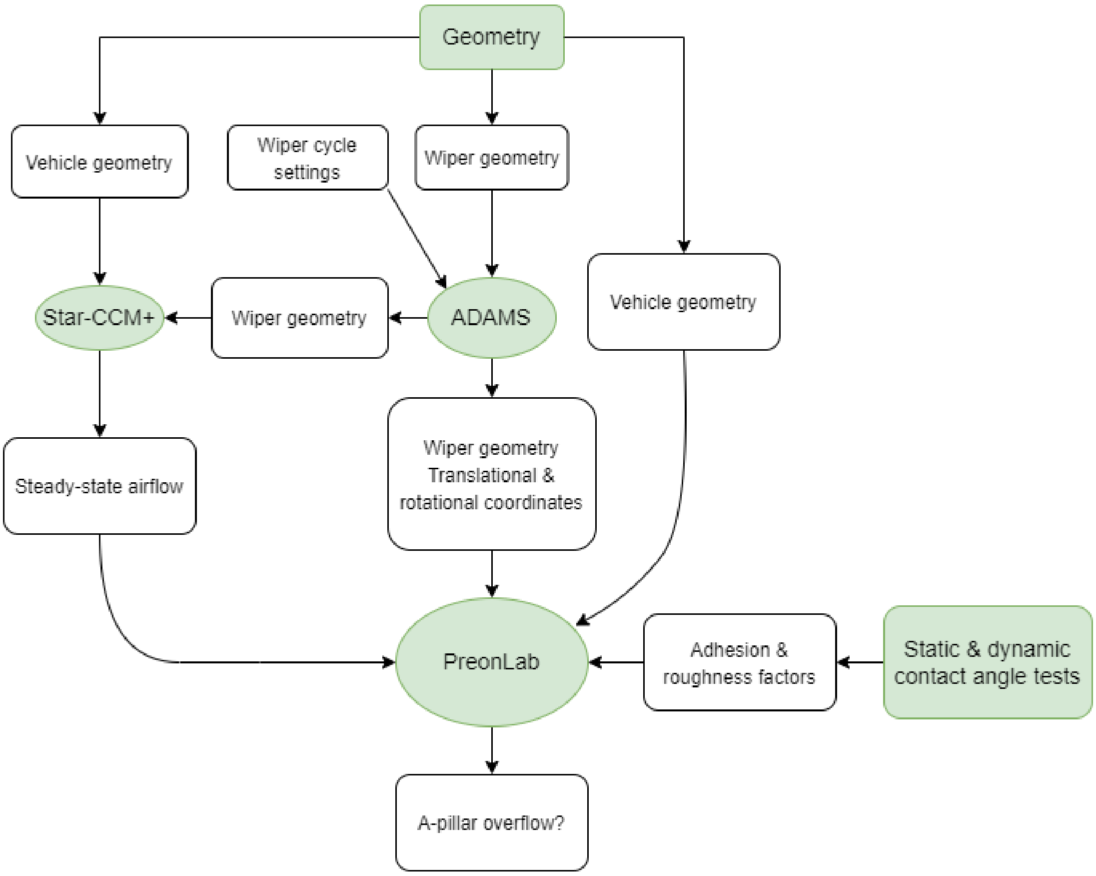

Figure 3.1: Flowchart of the process used to simulate A-pillar overflow

From Figure 3.1 there are five blocks in the colour green, and each is presented in its own section. The ellipse shaped blocks are the different software used, with the exclusion of CATIA which was used to split the wiper geometry, and ANSA which was used to repair the geometry before use in Star-CCM+ and ADAMS. The blocks coloured in white show input or output from the different blocks. For example, *Geometry* contains all geometry but only the *Vehicle geometry* is used in Star-CCM+ without pre-processing in ADAMS, while the *wiper geometry* is imported from ADAMS into Star-CCM+.

3.1 Geometry

The first vehicle model used in the thesis is a Volvo V90. The V90 is a mid-size station wagon. Prior physical tests have been done on A-pillar overflow on the V90 and the group had the vehicle easily available in case more tests were needed.

For the later stages of the thesis another vehicle model was introduced to test the SPH simulation model on. The vehicle model introduced was the XC40, a subcompact crossover SUV. As was the case with the V90 previous tests have been done on the XC40. The reason for the addition of another vehicle model is that the V90 has low amounts of A-pillar overflow and testing the SPH simulation on a model with more A-pillar overflow could determine how the simulation model predicts A-pillar overflow for two different scenarios.

3.2 PreonLab

The SPH solver used in the thesis was PreonLab by Fifty2. There are other commercial software used in the industry, but PreonLab is one of the more known. The Contamination & CFD group at Volvo Cars has a lot of in-house experience in working with PreonLab and some methods are already developed for the software. Since SPH is quite new in terms of industrial CFD there are a lot fewer options to choose from when it comes to solver settings.

The physics behind the solver is mostly explained in Chapter 2, but the details in the implementation are not. The company Fifty2 was founded in 2015 by Jens Cornelis and Markus Ihmsen, the SPH software PreonLab was the product of their research work. It is likely that the implemented SPH solver can be derived from the mix of research papers produced by Markus Ihmsen and Jens Cornelis.

The settings in PreonLab that are believed to be of particular interest for this thesis are the following:

- *Particle size:* the size of each individual particle.
- *Rest density:* the density of the fluid used, for this thesis two densities were used: 998.2071 kg/m^3 (water) and 958 kg/m^3 (wiper fluid)
- *No gap:* No gap determines how large the solid particles that make up the geometry used, if no gap is enabled the solids are modelled using half of the particle size to better capture small gaps. This increased ability to capture small gaps comes at a large computational cost, as halving the size of a particle increases the computational time by a factor of 8. Both *No gap* enabled and disabled were used throughout the thesis.
- *Cohesion model:* three models for cohesion are available: PreonCohesion, PairwiseForce and PotentialForce. In this thesis PotentialForce is used exclusively as it is the recommended cohesion model by Fifty2. Both the PairwiseForce and PotentialForce models are based on the Pairwise Force model described in Section 2.2.5. The difference is that the PotentialForce model accounts for micro-fluidic behaviour, but no further explanation is offered. The PreonCohesion model is only kept for legacy reasons and is not recommended by Fifty2.
- *Adhesion & Roughness factor:* The adhesion factor determines how hydrophilic/hydrophobic a surface is. In PreonLab the fluids surface tension (cohesion) is multiplied by the solids adhesion factor to yield the solids surface tension. For example if the adhesion factor is 0.5 the interfacial surface energy becomes $0.072 N/m \cdot 0.5 = 0.036 N/m$. There is no physical meaning when applied in the PF model because of its implementation. The higher the adhesion factor of the solid, the more hydrophilic it is. It is assumed that the surface tension of the fluid itself is not important, but that the ratio between the components are. The surface tension of water is used for both the wiper fluid and the water

used in the simulations. The *roughness factor* is described as the total friction force between the fluid and the solid. Both factors impact how quickly a fluid spreads on a surface as high adhesion promotes wetting and low roughness decreases the friction force between the fluid particles closest to the surface.

3.3 Static contact angle experiment

The static contact angle experiment was carried out to investigate if the physics of a droplet residing on a surface could be captured. The easiest, and most important, property is the contact angle which indirectly is a measurement of how hydrophobic a surface is. Since each solid material and fluid used will result in a different contact angle several combinations were tested. The materials tested were those in close proximity with the wiper fluid during a wiper cycle. The fluids tested were the standard concentration of 33 vol-% wiper fluid and 67 vol-% water, regular tap water and different wiper fluid concentrations. The reason was to study the impact that both wiper fluid and material had on the surface properties.

The following material samples were collected from a 2019 Volvo V90 Cross-Country: A-pillar moulding (APM), chrome trim from the door frame construction, rubber sealing trim between A-pillar and chrome trim. A rear passenger window from a Volvo V90 (year unknown) was in the department's possession and was also measured. The rear passenger window has two sides and depending on the glass used the sides have different surface tension, i.e the sides will be referred to as "Glass A" and "Glass B".

The experiment was conducted using seven different mixtures, where five were mixed by hand using graduated cylinders and a small cup. Each mixture was then stored in a marked cup and had its own single-use pipette. The mixtures tested were:

- 33 vol-% wiper fluid + 67 vol-% water and a drop of UV detection additive
- 50 vol-% wiper fluid + 50 vol-% water and a drop of UV detection additive
- Water
- Water and a drop of UV detection additive
- 33 vol-% wiper fluid + 67 vol-% water
- 50 vol-% wiper fluid + 50 vol-%
- Pre-made generic wiper fluid mixture from a company fuel station

The wiper fluid used for mixing is the OEM wiper fluid that all Volvo Cars vehicles use from the factory, (*Volvo Windscreen Washer Fluid*). The one received from the company fuel station is believed to be a 33 vol-% wiper fluid of another type.

The measurements were carried out indoors at ambient temperature (around 20° C) using a Dino-light USB microscope (calibrated according to the manual using a reference scale) and a stand with a coordinate table. Different backgrounds, such as paper with different colouring, were used in order to achieve high contrast between the background, the droplet and the surface of the material. All of the materials were cleaned before and in between each measurement using water and dry paper. An example of a measurement can be seen in Figure 3.2.

Figure 3.2: Droplet of 50 vol-% water/wiper fluid on rubber trim

To simulate the droplet a quadratic volume source box, filled with water, was placed on a flat plane in PreonLab. The size of the volume box was $5mm \cdot 5mm \cdot 5mm$ large. Four different particle sizes were tested: 0.5mm, 0.25mm, 0.125mm and 0.0625mm. Several different adhesion factors and roughness factors were tested. When the different adhesion factors were tested the roughness was fixed and vice versa. Since the droplet size was the same but the particle size was changed, the number of particles used to model a droplet was different between the cases. By changing the size of the volume source box the number of particles used could be constant between the different particle sizes. The reference number of particles chosen were 64 000 (corresponding to $5mm \cdot 5mm \cdot 5mm$ at a particle size of 0.125mm), due to computational reasons. The measurements were carried out by extracting a cross-section and by measuring the angle between the reference plane and the tangent between the triple point and the droplet. In the case of a low contact angle both the particle and the rendered representation of the droplet were used and compared. An example can be seen in Figure 3.3.

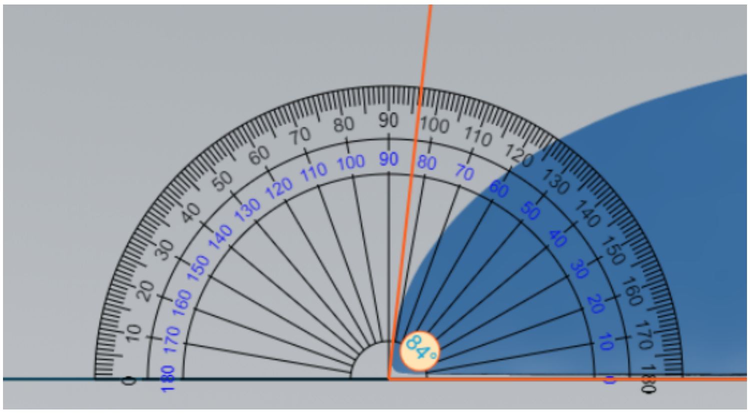

Figure 3.3: Measured contact angle on droplet with particle size 0.125mm and adhesion factor 0.8

3.4 Dynamic droplet behaviour study

To increase the knowledge about how the droplets behave dynamically in contact with surfaces, the study *"Droplet behaviors on inclined surfaces with dynamic contact* *angles"* by Jian Mengcheng and Zhou Biao was replicated [8]. The study included a physical test and the modelling of droplets using VOF. In the study a way of modelling advancing and retracting contact angles of impacting droplets was investigated, by also performing a physical experiment the authors were able to validate their implemented model. In the physical experiment the authors released a droplet from height onto an inclined surface. The impact was captured with a camera. In this thesis the resulting pictures from the physical experiment in the study were compared to the result derived from the PreonLab simulations. In Figure 3.4 for *Case 1* the properties of the droplet and the surface used in the physical experiment are found. *Case 1* was chosen as the reference for several reasons: liquid is water, low impact angle, glass as surface material, low input static contact angle (for comparing the CFD results from the study with the results from this thesis), low Weber number and low impact velocity. Water being used as the liquid is important since the fluid properties are known and water is used in PreonLab for these simulations. A low impact angle is believed to be important since the aim of the PreonLab simulations is to capture the dynamic behaviour of the fluid flowing across the surface and not have to consider what happens with a more aggressive impact, which a larger impact angle might have. The surface material of glass is closer in static contact angle to that of the windscreen used on the vehicle models, see Section 4.1. A lower Weber number is believed to be better since a lower value should have a smaller effect on the droplet from the impact.

Table 1 – Detailed liquid property, surface wettability and impact velocity for selected cases [19].

Case #	Liquid	Initial droplet diameter D (mm)	Impact angle α (°)	Viscosity μ (mPa·s)	Surface material	Input SCA (°)	Weber number (We)	Impact velocity V_p (m/s)
1	Water	2.7	10	1.0	Smooth glass	8	50	1.163
2	Water	2.7	10	1.0	Smooth glass	8	161	2.088
3	Water	2.7	10	1.0	Smooth glass	8	391	3.253
4	Water	2.7	10	1.0	Wax	100	50	1.163
5	Water	2.7	10	1.0	Wax	100	161	2.088
6	Water	2.7	10	1.0	Wax	100	391	3.253
7	Water	2.7	9.5	1.0	Smooth glass	8	50	1.163
8	Water	2.7	20	1.0	Smooth glass	8	50	1.163
9	Water	2.7	5	1.0	Wax	100	50	1.163
10	Water	2.7	20	1.0	Wax	100	50	1.163
11	Glycerin	2.45	9	Varied	Smooth glass	15	51	1.037

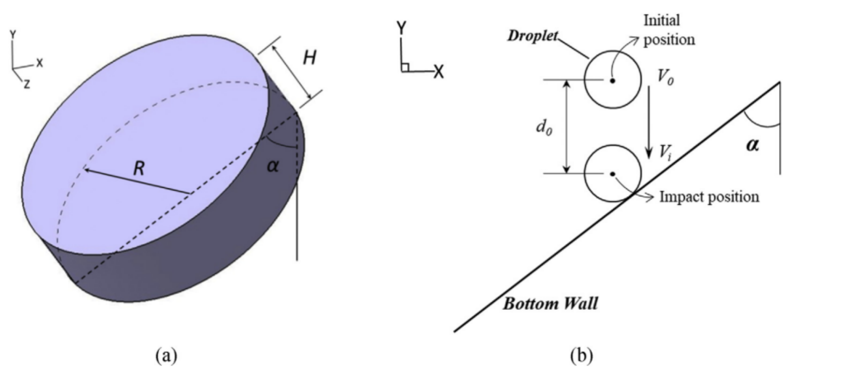

Figure 3.4: The properties of the reference study with a table over the different cases tested, (a) - Showing the computational domain, (b) - 2D schematics of the experiment. *Source: "Droplet behaviours on inclined surfaces with dynamic contact angles*[8]

The parameters investigated in PreonLab were: particle diameter, droplet size, surface adhesion and surface roughness. By replicating and comparing the study, a comparison between the parameters could be performed by using the photos showing the droplets at different time instances from impact. There was also a spreading factor, l/D that was derived from the results of the computational model in the study. The spreading factor was the measured distance from the trailing to the leading edge of the droplet. To account for the time, a unitless number was used, t^*, see Equation 3.1.

$$t^* = t\frac{V_p}{D} \tag{3.1}$$

Where t is the time from impact, V_p is the velocity at impact and D is the droplet diameter before impact.

The settings used in the PreonLab simulations were the following:

- *Liquid properties:* Water
- *Particle Sizing:* 0.025mm, 0.125mm
- *Droplet resolution:* 5 242 (particle size: 0.125mm)
- *Volume source box:* $2.176mm \cdot 2.176mm \cdot 2.176mm$
- *Impact velocity:* 1.1626m/s
- *Weber number:* 48.9

A droplet size sensitivity comparison was also conducted by using the settings:

- *Liquid properties:* Water
- *Particle Sizing:* 0.125mm
- *Droplet resolution:* 64 000
- *Volume source box:* $5.00mm \cdot 5.00mm \cdot 5.00mm$
- *Impact velocity:* 0.7909m/s
- *Weber number:* 52.19

3.5 Airflow modelling

A conclusion from physical windscreen washing tests is that the most prominent forces on the liquid are those induced by the airflow. It is believed that it is crucial that the airflow modelling is complex enough to capture the most important differences in pressure around the windscreen and A-pillar region. Since the overall workflow for the final simulation model needs to be less complicated than the current one, see Section 1.1, and the importance of the different pressures around the windscreen and A-pillar are not fully investigated a simplified approach was used. The airflows implemented in PreonLab will be time-averaged and from CFD simulations at different static positions. The pressure distributions that are believed to be of most importance for A-pillar overflow are the general high pressure around the A-pillar region, the locally lower pressure behind each of the wipers and the lower pressure around the A-pillar when the wipers are in the top position. The general high pressure around the A-pillar is prominent during most of the wiper cycle and derived in this thesis from when the wipers are in the parked position. The locally lower pressure behind the wipers is a constant phenomena occurring throughout the whole wiping cycle and is derived from when the wipers are at an angle approximately 45° or 60°, depending on vehicle model, from the DS wiper start position, measured at the DS wiper shaft. The angle was chosen because this was the angle that had the lowest pressure behind the DS wiper. The lower pressure around the A-pillar occurs as the DS wiper approaches the top position.

The airflow implementation in PreonLab was done in three main configurations, with the most basic configuration using one overall airflow. Figure 3.5 shows the parked wiper position which the overall airflow was derived from.

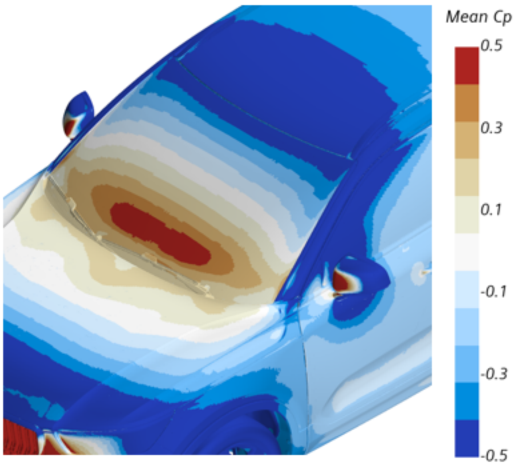

Figure 3.5: Wipers set in parked position

The second main configuration uses two overall airflows with different activation times. The use of activation time makes it possible to apply certain airflows at certain times. In this application, it is used to apply the airflow derived from a parked position at all times, except for when the wipers are approaching the top position. Around the top position, an airflow derived from simulations at the top wiper position is active. Figure 3.6 presents the two positions used at which the airflows were derived.

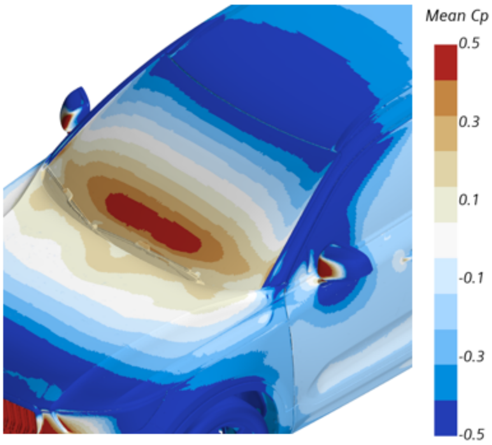

(a) Parked wiper position (b) Top wiper position

Figure 3.6: The two positions used during a wiper cycle, left figure showing the parked/bottom position and the right figure showing the top position

For the third main configuration, two overall airflows were used and additional local airflows around the wiper blades were added. The overall airflows were implemented as described for the second main configuration. The DS wiper output shaft angle chosen for the airflow derivation was from approximately 45° for the V90 and 60° for the XC40. Figure 3.7 shows the different wiper positions used for the XC40 simulations.

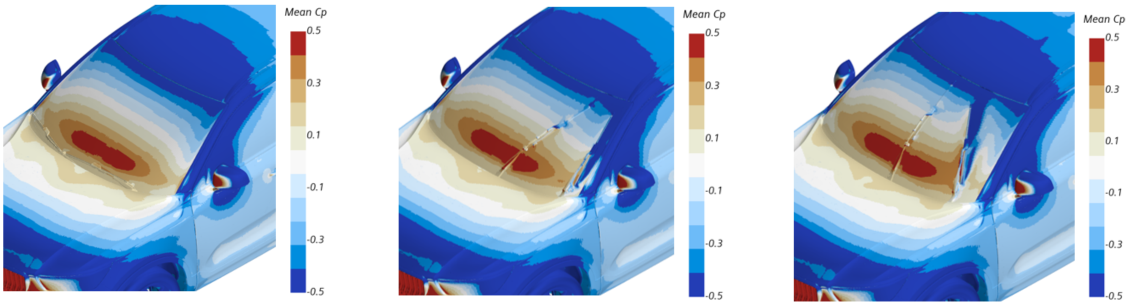

(a) Parked wiper position (b) Top wiper position (c) 60° wiper position

Figure 3.7: The three positions used during a wiper cycle, left figure showing the parked/bottom position, middle figure showing the top position and the right figure showing the wiper position for the local airflows around the wiper

The airflow implementation for the localised airflows around the wipers was limited to smaller boxes around the wipers in PreonLab. The size of the boxes were only as large as needed to cover most of the low pressure wake around the wiper, see Figure 3.7. There are differences between the box sizes used in the V90 and the XC40 simulations because of the differences in geometry between the wipers, as well as how the importance of the box size changed when going from the V90 to the XC40 model. The last iteration of box size is shown in Figure 3.8, where the box size has the dimensions $8.67 \cdot 66.5 \cdot 7.83$cm for the DS wiper and $8.67 \cdot 52.0 \cdot 7.83$cm for the PS wiper.

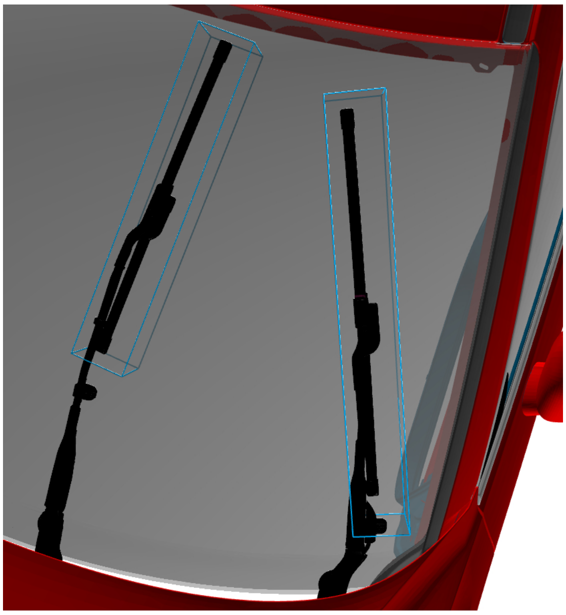

Figure 3.8: The airflow imported in PreonLab at the same position as the aerodynamic simulation was run.

The same setup for the airflow implementation was used for the Volvo XC40 in the PreonLab simulations.

The aerodynamic simulations were run according to an in-house developed standard at 70km/h for the Volvo V90 and 80km/h for the Volvo XC40. The velocities chosen for each vehicle model were determined from which velocity that created the most A-pillar overflow in the physical tests. The mesh in the CFD simulations consists of approximately 260 million cells. The final results are achieved from a transient simulation using Improved Delayed Detached Eddy Simulation (IDDES). Since the airflows used in PreonLab simulations are steady-state, the velocities in the CFD simulations are averaged for a set time after the solution is considered stabilized. The CFD simulations follow the in-house developed method and the averaged airflows are exported using the centroid position of each cell and its velocity components in the cartesian system.

3.6 Wiper kinematics modelling

The wipers were modelled using a multibody dynamic simulation software called ADAMS. The software has the ability to model systems of rigid and flexible bodies. ADAMS was used due to it being one of the leading multibody dynamics simulation software available and it has a wide use within the automotive industry, particularly within suspension kinematics modelling.

The wiper simulation was set up by importing the windscreen and wipers into the software and applying the correct joints, springs between wiper arm and wiper blade, and friction contact between the wiper blade and the windscreen. Since the windscreen has different curvature at different points, the wiper blades were modelled using a simple beam model called *flexible beam model*, in ADAMS. By doing so the wiper blade curvature adapts to the windscreen and stays in contact as the wiper blade moves.

The SPH solver does not support flexible beams from ADAMS which meant that the wiper blade had to be split into several smaller rigid elements, using CAD software, which then were exported to PreonLab. All separate parts in ADAMS have their own center of mass. By measuring the orientation and coordinates of this center of mass the movement of the parts can be extracted and imported into PreonLab.

At the beginning of the thesis work there was already a wiper setup in ADAMS available and a workflow established on exporting the data from ADAMS. The same workflow and setup was continuously used throughout the thesis, while adding or changing parts of it (for example friction or normal force, changing windshield or wiper geometry).

3.7 Static car wiper experiment

A wiper test on the Volvo V90 without the influence of an external airflow was conducted in order to validate the liquid and surface properties. The experiment was conducted indoors. Only two fluids were tested: water with drops of a UV detection additive and 33/67 vol-% wiper fluid/water and drops of the UV detection additive. The low voltage system of the car was supported by an external charger with the engine turned off. A camera recorded the fluid as it moved across the windscreen. The same wiping cycle was used as the one used in the SPH-simulations. It was repeated twice for each fluid as two positions for the camera were used in order to capture the A-pillar region and the overall flow on the windscreen.

The recordings were analysed qualitatively to approximate the movement of the bulk liquid. The liquid movement could be visually traced by using air bubbles stuck in the liquid and the distributional change of reflective light and the size of the wet area.

To approximate the mass flow of each injector a separate test on only the DS wiper was conducted. By injecting the wiper fluid, using the same wiper cycle as in the PreonLab simulations, and leading the ejected fluid into a graduated cylinder the amount of injected liquid on the driver side could be measured. The assumption is that each injector outputs equal amounts of fluid. For the SPH simulations it is assumed that the passenger side suffers similar pressure loss as the driver side and that the passenger side ejector massflow can be approximated from the driver side.

3.8 A-Pillar Overflow Simulations

3.8.1 V90

The wiper simulations were first run without airflow using the Volvo V90. A static wiper experiment was performed to validate the wiper simulation, see Section 3.7. After this, a steady-state airflow was introduced to investigate the effect on the fluid behaviour. The aim was to remove the need of running a transient wiper simulation using standard FVM CFD but still capturing the low pressure wake behind the wiper blades.

The surface properties used in the early stages of the project, were the same properties derived from the static contact angle and dynamic droplet behaviour studies presented in Sections 4.1-4.2 respectively. The approach was to run simulations and only change one property at a time, analyse the results by looking at different characteristics of the fluid behaviour and then run a new simulation with the changes applied. A compilation of the simulation settings tested is presented in Table 3.1.

Table 3.1: The differences between the simulations run for the static V90 simulations

V90 - Static						
Simulation	Particle Size [mm]	Windshield Adh/Ro	Painted Steel Adh/Ro	APM Adh/Ro	Wiperblade Adh/Ro	Liquid
1	0.125	1.6/2	0.65/1	1.4/1	1.4/1	Water
4	0.125	1.6/0.5	0.65/1	1.4/1	0.65/1	Water
5	0.125	1.6/1	0.65/1	1.4/1	0.65/1	Water
6	0.125	1.6/0.1	0.65/1	1.4/1	0.65/1	Water
10	0.125	1.2/1	0.65/1	1.4/1	0.65/1	Water
11	0.125	1/1	0.65/1	1.4/1	0.65/1	Water
12	0.125	1.2/0.5	0.65/1	1.4/1	0.65/1	Water

After performing the static PreonLab simulations, the implementation of airflow was introduced.

The simulations with airflow implemented are denoted: *A1 V90, A2 V90,...,An V90*, and Table 3.2 shows all simulations with airflow implemented. All simulations with airflow were run using Iteration 12 in Table 3.1 as the baseline simulation. In column $Airflows$ in Table 3.2 the duration of the airflow at the top wiper position is denoted as $(+-x\,ms)$ from the top wiper position. The fluid in the static simulations used the properties of water but the final PreonLab model should use the properties of the OEM wiper fluid, therefore, a switch to the properties of the wiper fluid was done for simulation A2 V90. A1 V90 then serves as the reference and any difference in fluid behaviour between A1 V90 and A2 V90 is due to the fluid properties.

Table 3.2: Simulations run for the V90 with airflow implementation

V90 - With airflow implemented										
Simulation	Particle Size [mm]	Velocity [km/h]	Windshield Adh/Ro	Painted Steel Adh/Ro	APM Adh/Ro	Wiperblade Adh/Ro	Airflows	Airflow Scaling	Gravitational acceleration [$\frac{m}{s^2}$]	Liquid
A1 V90	0.125	70	1.2/0.5	0.65/1	1.4/1	0.65/1	Parked + Top (+/-200ms) + 45 degree DS wiper	1	9.81	Water
A2 V90	0.125	70	1.2/0.5	0.65/1	0.65/1	0.65/1	Parked + Top (+/-200ms) + 45 degree DS wiper	1	9.81	Windscreen Washing Liquid
A3 V90	0.125	70	1.2/0.5	0.65/1	0.65/1	0.65/1	Parked	1.5	9.81	Windscreen Washing Liquid
A4 V90	0.125	70	1.2/0.5	0.65/1	0.8/1	0.65/1	Parked + Top (+/-200ms) + 45 degree DS wiper	1	7.0	Windscreen Washing Liquid
A5 V90	0.125	70	1.2/0.5	0.65/1	0.8/1	0.65/1	Parked + Top (+/-100ms) + 45 degree DS wiper	1.5	9.81	Windscreen Washing Liquid
A6 V90	0.125	70	1.2/0.5	0.65/1	1/0.5	0.65/1	Parked + Top (+/-100ms) + 45 degree DS wiper	1.5	9.81	Windscreen Washing Liquid

3.8.2 XC40

The XC40 PreonLab model was set up in the same way as the V90 simulations. The approach was similar, with the exception that no static vehicle experiment was conducted. At first, a single simulation without the airflow was run to verify that the kinematics and the overall behaviour of the fluid were correct.

The XC40 PreonLab model was set up using the V90 simulation model as a reference. What differentiates the V90 simulation model from the XC40 simulation model is the geometry, wiper kinematics and injectors. To trigger A-pillar overflow at an earlier stage the injection cycle was changed to injecting wiper fluid continuously. The wiper kinematics were modelled in ADAMS, using angular velocity data from the manufacturer. The position of the injectors were located from the CAD model and the spray angles of the injectors were derived from a video of the wiping cycle with the vehicle at a standstill. The actual injection velocity for each injector was available from a previous measurement.

A simulation without airflow implemented was run to verify that the correct settings had been applied and that the overall behaviour of the fluid looked visibly correct. The injection velocity used was scaled by a factor of 0.65 to reduce the computational cost as the time steps increased while fulfilling the CFL requirement. The injection area of the injectors was adjusted to attain the correct massflow. After the static vehicle simulations a series of simulations with airflow implemented were run using the scaled injection velocity. An excerpt of the simulations run can be seen in Table 3.3.

Table 3.3: List of simulations performed for the XC40

XC40 - Simulation list									
Simulation	Particle Size [mm]	Velocity $[\frac{km}{h}]$	Windshield Adh/Ro	Painted Steel Adh/Ro	APM Adh/Ro	Wiperblade Adh/Ro	Airflows	Air density scaling	Liquid
1 XC40	0.125	-	1.2/0.5	0.65/1	0.8/1	0.65/1	-	-	Windscreen Washing Liquid
2 XC40	0.125	-	1.2/0.5	0.65/1	0.8/1	0.65/1	-	-	Windscreen Washing Liquid
3 XC40	0.125	-	1.3/0.5	0.65/1	0.8/1	0.65/1	-	-	Windscreen Washing Liquid
A1 XC40	0.125	80	1.2/0.5	0.65/1	0.8/1	0.65/1	Parked + Top (+/-100ms) + 60 degree PS+DS wiper	2.25	Windscreen Washing Liquid
A2 XC40	0.125	80	1.2/0.5	1.2/0.5	1.2/0.5	0.65/1	Parked + Top (+/-100ms) + 60 degree PS+DS wiper	2.25	Windscreen Washing Liquid
A3 XC40	0.125	80	1.2/0.5	1.2/0.5	1/0.5	0.65/1	Parked + Top (+/-100ms) + 60 degree PS+DS wiper	2.25	Windscreen Washing Liquid

4

Results & Discussion

4.1 Contact angles

The measurements from the static contact angle experiment is presented in table 4.1.

Table 4.1: Static contact angles for different mixtures and materials

	Measured contact angles, [θ]									
	Rubber trim		A-pillar moulding		Chrome trim		Glas A		Glas B	
33/67 + UV	25	24	50	49	6	6	-	-	12	11
50/50 + UV	24	23	50	47	6	6	-	-	-	-
Water	87	89	97	101	50	47	19	19	30	33
Water + UV	87	88	91	92	55	57	-	-	-	-
33/67	37	31	36	42	13	18	-	-	-	-
50/50	24	21	40	39	-*	-*	-	-	-	-
From Supply	37	41	45	48	33	29	16	14	19	22

*No measurement was taken as contact angle was too small

Table 4.1 highlights that each fluid and material combination has a range of static contact angles, as the left and right measurement often differs. The exact static contact angle is not of particular interest as the aim of the measurement is to get a ballpark number, to be used in the simulation. It is assumed that the *Glas A* static contact angle for *33/67 vol-% + UV* is of particular interest, but the measurement was missed. As further studies were performed, see Section 4.3.4, it became clear that the measurement would not be needed.

From the first sweep, using the same quadratic volume source, of adhesion factors the contact angles were compiled in Figure 4.1.

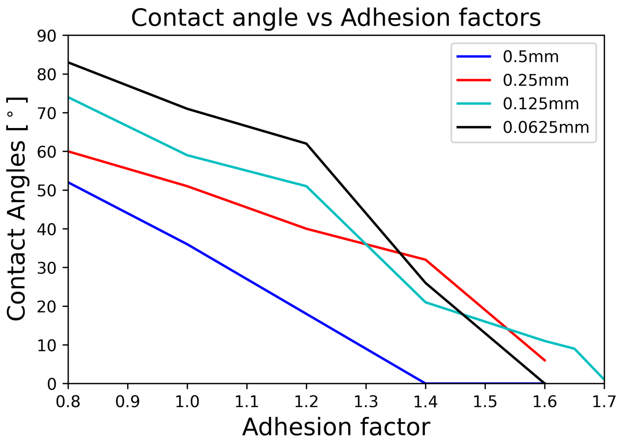

Figure 4.1: Contact angle as a function of Adhesion factor sweep

In Figure 4.1 the y-axis shows the contact angles, x-axis the adhesion factor and each isoline represents one of the four particle sizes: 0.5, 0.25, 0.125 and 0.0625mm.

From Figure 4.1 it is clear that the static contact angle and adhesion factor follow a linear behaviour. It is noted that smaller particle size for a given adhesion factor results in a larger static contact angle, i.e smaller particle size results in a less hydrophilic surface.

Then particle resolution was tested for differently sized volume sources to get 64 000 particles in resolution for a droplet. In Figure 4.2, the particle size is 0.5mm in diameter for the red and black isoline. The last isoline represents the reference, the 0.125mm particle diameter.

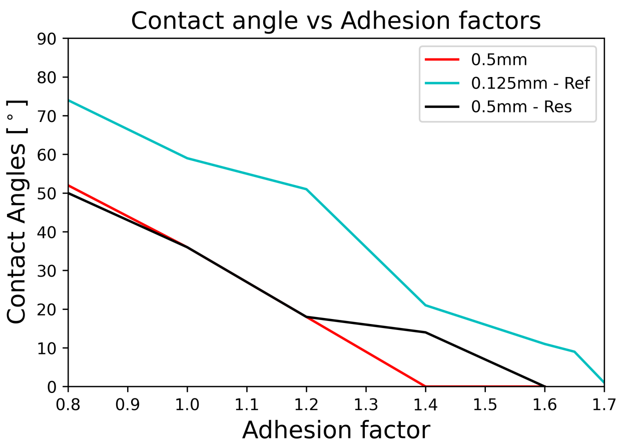

Figure 4.2: Contact angle as a function of adhesion factor for differently resolved droplets at particle size 0.5mm

Note in Figure 4.2 there is an additional measurement point since the larger resolution allowed for smaller contact angles to be captured. For all static angles for the 0.5mm particle size, the difference in resolution is negligible.

Figure 4.3 shows the 0.25mm particle size together with the reference diameter of 0.125mm.

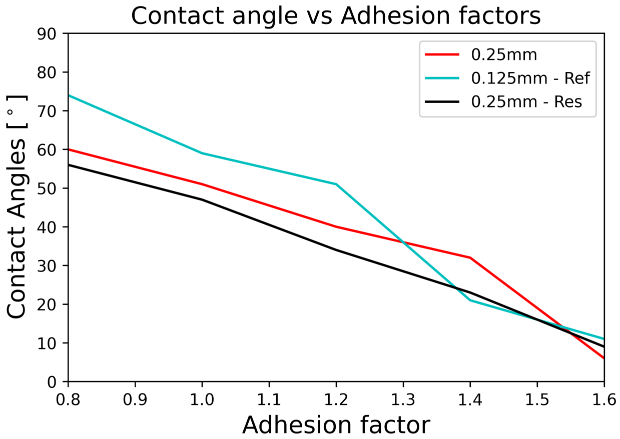

Figure 4.3: Contact angle vs adhesion factor for differently resolved droplets for particle size 0.25mm

In Figure 4.3 the contact angle is slightly larger for the coarser resolved droplet, but the difference is small.
The last case tested with varying volume source is the 0.0625mm in particle diameter, the result can be found in Figure 4.4. Since the 0.125mm particle size is larger than the 0.0625mm, this droplet has a coarser resolution.

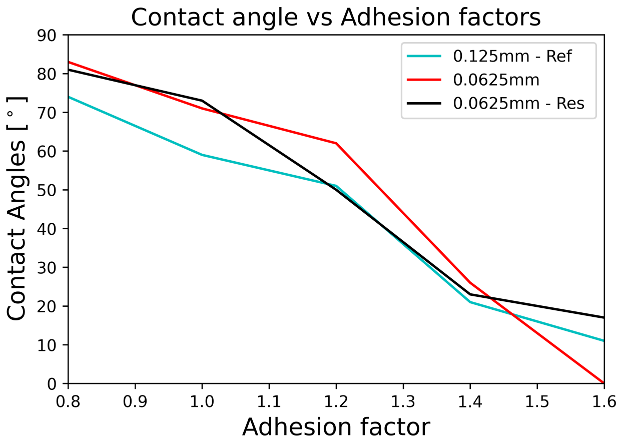

Figure 4.4: Contact angle vs adhesion factor for differently resolved droplets for particle size 0.0625mm

In Figure 4.4 the contact angles are starting to converge. The difference between the smaller and normal resolution of 0.0625mm is small.

To rule out that the droplet resolution is not the cause of the lower contact angle in Figure 4.1, both Figure 4.2, Figure 4.3 and Figure 4.4 support this conclusion. In Figure 4.2 it is observed that the higher resolution enabled an additional measurement. For adhesion factor up until 1.2 there is no difference between the coarser or the finer droplet resolution. In Figure 4.3 the higher resolution droplet consisting of particle size 0.25mm rendered a slightly lower contact angle for the same adhesion factor. For the smallest particle size of 0.0625mm, there is no visible difference between the more resolved droplet and the coarser droplet, as seen in Figure 4.4. The finer resolved droplet enabled an additional measurement, similar to the finer resolved droplet for the 0.5mm particle size.

4.2 Dynamic droplet behaviour

The adhesion sweep, using the adhesion factors: 0.6, 0.8, 1, 1.2, 1.4 and 1.6, is seen in Figure 4.5. The particle sizing used is 0.125mm.

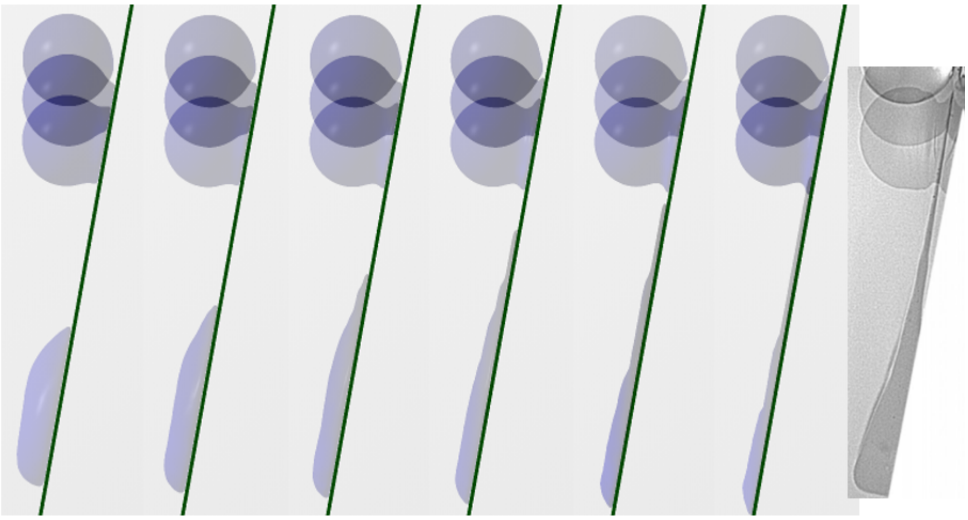

Figure 4.5: Adhesion sweep, with reference from study to the right, using particle size 0.125mm[8]. Adhesion factors from left: 0.6, 0.8, 1, 1.2, 1.4 and 1.6

In Figure 4.5 there are noticeable steps in the droplet silhouette, especially visible in the adhesion span: 1-1.6. There is a visible difference in spreading between the simulated droplets and the physical droplet. For particle sizing 0.125mm an adhesion factor of 1.2 seems to capture the overall shape of the droplet best. The velocity of the simulated droplets is larger than the velocity of the droplet in the physical experiment.

The two parameters that affect surface velocity are the adhesion and roughness factor, as described in Section 3.2. Both work in conjunction with each other. For example, a large adhesion factor will make the droplet more hydrophilic, causing it to flow quicker across the surface, as seen in Figure 4.5. A lowered roughness factor will create less friction and allow for more sliding. To reduce the velocity of the droplet a larger roughness factor could be tested. There is a step for all simulated droplets where there is interaction with the surface, this seems to be a result of the impacting droplet pushing its particles in front of it as it descends. This behaviour is not the case with the physical experiment. The fluid of the droplet interacting with the surface might stick and the bulk flow of the droplet has a larger downward facing velocity. Another possible explanation could be that the droplet is rolling on the surface.

The adhesion sweep, using the adhesion factors: 0.6, 0.8, 1, 1.2, 1.4 and 1.6, is seen in Figure 4.6. The particle sizing used is 0.025mm.

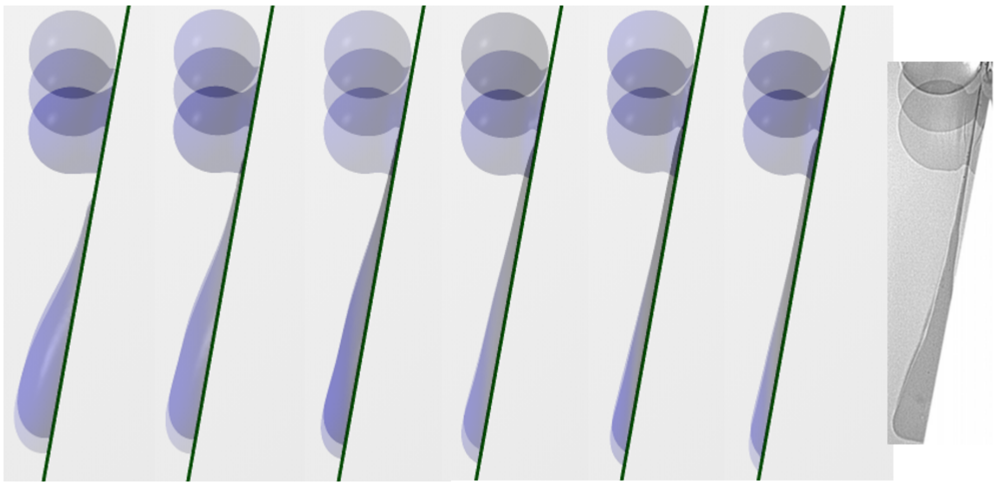

Figure 4.6: Adhesion sweep, with reference to the right, using particle size 0.025mm[8]. Adhesion factors from left: 0.6, 0.8, 1, 1.2, 1.4 and 1.6

In Figure 4.6 the last two shadows represent the time-step before and after 9ms. The contour of the simulated droplet at 9ms is a combination of the two.

Figure 4.6 highlights the importance of correct time measurements as the two overlayed shadows of each adhesion factor show the interpolation of a time-step of 0.25ms before and 0.25ms after 9ms, the lightly shadowed area shows the leading edge movement corresponding to 0.5ms. The adhesion factor that captures the overall behaviour best seems to be adhesion factor 1.2 or 1.4. Adhesion factor 1.2 has an almost flat "back" (curvature from the highest point of the droplet perpendicular from the surface to the trailing edge), and quite large advancing contact angle (contact angle at leading edge). Adhesion factor 1.4 has a completely flat back, but the highest point is really low compared with the experimental photo.

The spreading factor, l/D, for particle size 0.125mm, with three different adhesion factors, can be found in Figure 4.7.

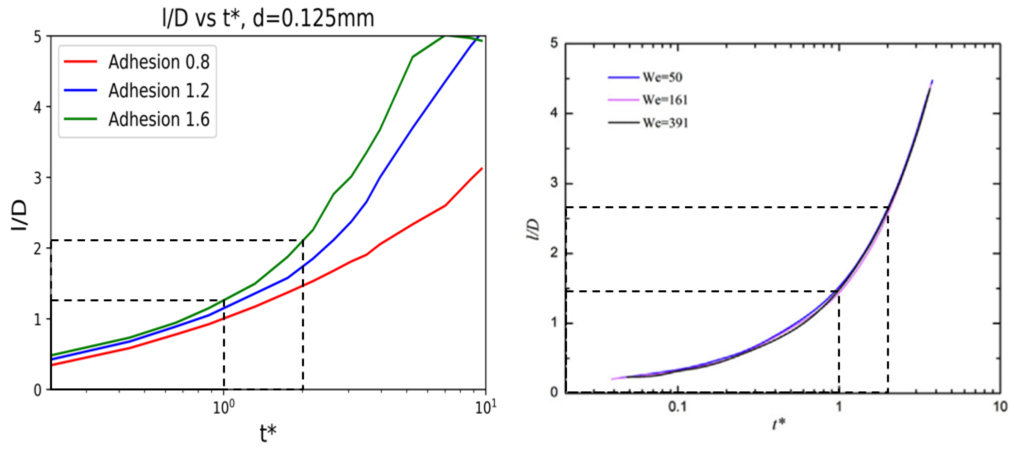

Figure 4.7: Spreading factor for three adhesion factors with particle size 0.125mm to the left, reference from study to the right[8].

Spreading factor for particle size 0.025mm, with three different adhesion factors, can be seen in Figure 4.8.

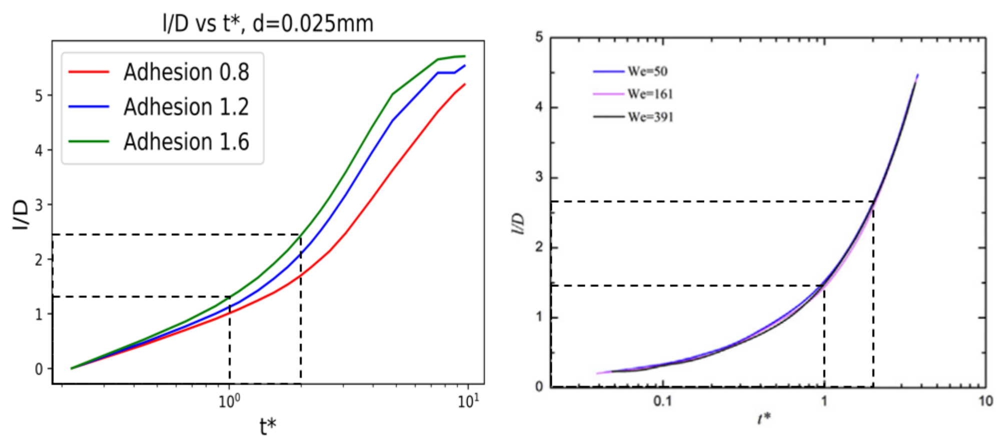

Figure 4.8: Spreading factor for three adhesion factors with particle size 0.025mm to the left, reference from study to the right[8].

Roughness factor was tested for particle size 0.125mm. The result can be viewed in Figure 4.9

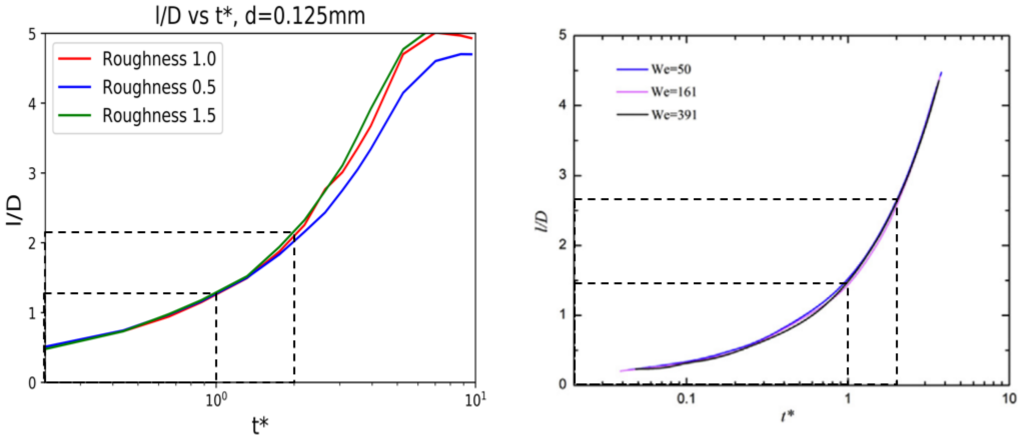

Figure 4.9: Spreading factor for three roughness factors tested for particle size 0.125mm to the left, reference from study to the right[8].

In Figure 4.7 and Figure 4.8 a larger adhesion factor results in a larger spreading factor, for both particle sizes of 0.125mm and 0.025mm adhesion factor 1.6 captures the spreading factor better. The roughness factor was also tested, see Figure 4.9, and it affected the spreading factor a lot less than the adhesion factor. The conclusion is that the adhesion factor is the most important factor and should be the primary factor to change when testing different surface properties for the A-pillar overflow simulations.

4.3 A-pillar overflow simulations

Section 4.3 covers the different areas believed to be of importance for A-pillar overflow, including the subsections *Influence of adhesion/roughness factor*, *Influence of liquid properties*,*Influence of airflow parameters* and *Miscellaneous*. The results are presented in chronological order, thus often starting with the Volvo V90 simulations and then presenting the results from the Volvo XC40 simulations.

The first subsection *Influence of adhesion/roughness factor* presents the early results from the static V90 simulations and later the XC40 with liquid-airflow interaction implemented. The V90 results were used to derive the adhesion/roughness factors used for the windscreen. Then the results from the XC40 simulations, with airflow-liquid interaction, are presented as the adhesion/roughness factors for APM, A-pillar and chrome trim were set using the latter vehicle model.

The second subsection *Influence of liquid properties* contains results and discussion about the liquid properties in the A-pillar overflow simulations and a brief discussion about the connection between the results from the static and dynamic droplet studies and A-pillar overflow simulations.

The third subsection *Influence of airflow parameters* contains the results from the V90 simulations using the scaled velocity vector approach and the results from the

XC40 simulations using the density as a scaling parameter. A discussion about the airflow-liquid model used, the two tuning approaches, and the implications thereof is also included.

In the fourth subsection *Comparison of V90 and XC40* comparisons are made between the wind tunnel tests and final simulations of the two vehicle models.

In the last subsection *Miscellaneous* the simulation results that do not fit in the other subsections are presented.

4.3.1 Influence of adhesion/roughness factor

In the early Volvo V90 simulations, a static vehicle was used and the resulting windscreen adhesion/roughness factors were mainly derived from the results of iteration 1-12. Later, as the adhesion/roughness factors for the other materials were studied, an airflow-liquid model was introduced and the vehicle model studied was the XC40.

The physical test that the V90 simulations were compared with was a static windscreen washing event. The test used a 33 vol-% wiper fluid + UV and in Figure 4.10 there is a comparison between the start of the first downstroke and the second downstroke in the physical test.

(a) Wiper test at beginning of first downstroke

(b) Wiper test at beginning of second downstroke

Figure 4.10: Fluid pattern for wiper test at different time instances

Figure 4.10a has a noticeable larger spreading of wiper fluid at the passenger side wiper. Around the A-pillar region there is a larger coverage of wiper fluid in Figure 4.10b compared to Figure 4.10a, supported by the lack of fluid streaks between the driver side wiper and the APM in Figure 4.10b.

Iterations 1, 5, 10 with particle size 0.125mm have both differences in adhesion and roughness factors, see Table 3.1. Iterations 1, 5 and 10 are compared at the beginning of the first downstroke.

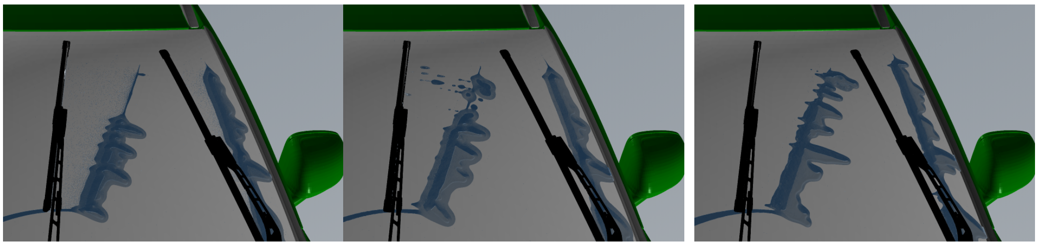

(a) Iteration 1 (b) Iteration 5 (c) Iteration 10

Figure 4.11: Fluid pattern development for 1, 5 and 10 at beginning of first downstroke

In Figure 4.11a there is a lack of pooling at the top of the passenger side wiper. In Figure 4.11b and Figure 4.11c there is pooling. When looking at the area around the A-pillar in Figure 4.11c there is an uneven contour of fluid that is not visible in Figure 4.11b. It is by looking at these results qualitatively and analysing them in a similar manner for the other simulations that the final adhesion/roughness factors were set for the windscreen.

Iterations 10 and 12 have the same value, 1.2, on windshield adhesion, but 1 and 0.5 in windshield roughness respectively. Iteration 11 shares the same windshield roughness as iteration 10, but a lower adhesion factor of 1. Figure 4.12 shows the beginning of the first downstroke for iterations 10, 11 and 12.

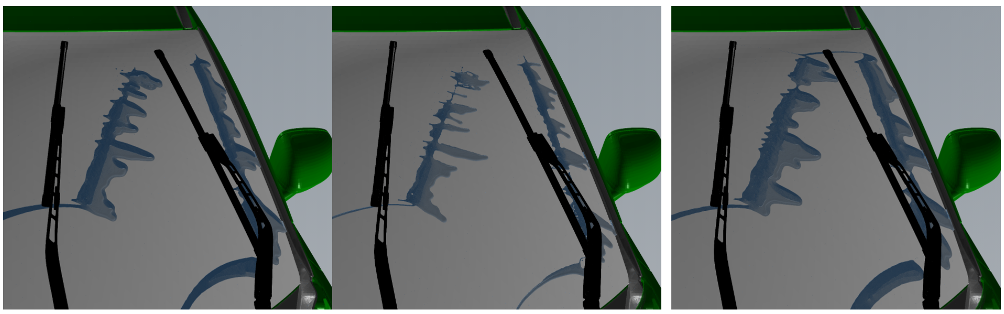

(a) Iteration 10 (b) Iteration 11 (c) Iteration 12

Figure 4.12: Fluid pattern for iterations 10, 11 and 12 at beginning of first downstroke

In Figure 4.12a and Figure 4.12c there is an uneven contour of spreading for the passenger side wiper pooling. Around the driver side wiper there are several streaks of fluid that reach the A-pillar for iteration 12 but not for iteration 10. There is also some overspray visible in iteration 12. For 11 in Figure 4.12b there are individual streaks of fluid everywhere on the windshield.

The most promising adhesion and roughness factor combination is 1.2 and 0.5 for each factor respectively. When comparing iteration 12 with these settings, Figure 4.12c, and the physical test at the same timestep, Figure 4.10a, there are notable differences. The A-pillar region in the physical test has more defined streaks, indicating less surface adhesion, as the momentum of the liquid carries the fluid across the windshield area between the A-pillar and the reversing point of the driver side wiper, which is not the case in iteration 12.

The adhesion and roughness factors chosen as starting points were adhesion factor: 1.6 and roughness factor: 1. From earlier discussions, see Section 4.1 and Section 4.2, a large adhesion factor was favored for all comparisons. The static contact angle favored for *Glass A* using water lies between 1.4-1.5 as this would result in a static contact angle of 20°. A smaller contact angle is believed to be appropriate if modelling wiper fluid, as *Glass B* had a static contact angle of 12° for the wiper fluid and *Glass A* would most probably have an even lower by comparing the static contact angles for water. Figure 4.5 shows that adhesion factor 1.2-1.4 would be suitable for *Smooth glass*, i.e similar to *Glass B* in Table 4.1. Contradictory, Figure 4.7 shows that a larger adhesion factor than 1.6 is needed when having *Smooth glass*.

In hindsight, a lower starting adhesion factor should have been used. The final adhesion factor of 1.2 for the static car simulations is a lot smaller than the starting value of 1.6 adhesion factor. The adhesion factor seems to determine both how quickly and where the wiper fluid spreads. By looking at some iterations with the same windshield roughness factor but different windshield adhesion factors this claim of how, where and the rate of spreading can be supported. In Figure 4.11b the adhesion is 1.6 and iteration 5 has an even spread along the A-pillar region and also even spread around the passenger side wiper when compared to iteration 11, see Figure 4.12b. When comparing iteration 5 in Figure 4.11b with iteration 10 in Figure 4.12a there is a noticeable difference around the A-pillar region with iteration 10 having significantly more defined streaks of wiper fluid. The passenger side wiper area is more even in Figure 4.11b than in iteration 10, see Figure 4.12a.

The roughness factor seems to have an effect on how quickly the fluid is spreading, and not so much on the spreading pattern. Note that from the comparisons all of the surface properties (adhesion and roughness factor) together with the particle sizing seems to affect each other to a different degree.

The tuning of adhesion/roughness factor for the APM and A-pillar were concluded from the XC40 simulations with airflow-liquid interaction. The A1 XC40 does not capture A-pillar overflow correctly as there are small amounts of overflow even after beginning the third downstroke, as shown in Figure 4.13 where a comparison between A1 XC40 and a wind tunnel test is made.

Figure 4.13: A1 XC40 and wind tunnel test at the beginning of the third downstroke

In Figure 4.13 in the middle of the A-pillar of the simulation there is barely any overflow when compared to the wind tunnel test. Since airflow-liquid interaction, see subsection 4.3.3, and the windshield surface properties have been tested, while the APM and A-pillar have not yet been investigated, a simulation using the same surface properties on the APM, A-pillar and chrome trim as used on the windscreen was run in A2 XC40.

A1 XC40 compared with A2 XC40 in Figure 4.14 where the wipers have completed half of the first downstroke.

Figure 4.14: A1 XC40 and A2 XC40 after completing half of the first downstroke

A1 XC40 compared with A2 XC40 in Figure 4.15 and the wipers have completed half of the second downstroke.

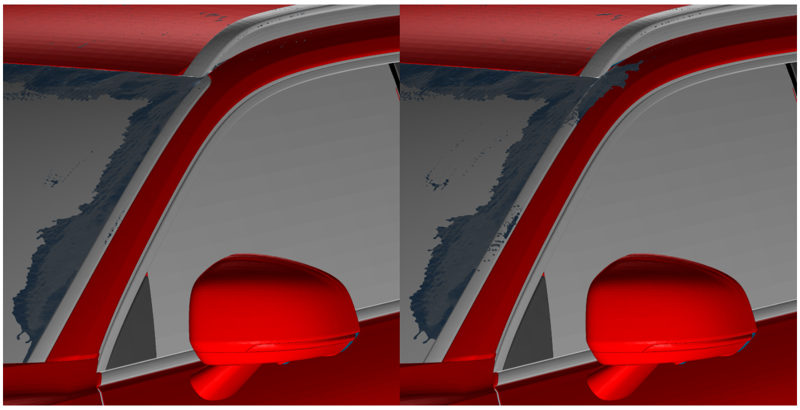

Figure 4.15: A1 XC40 and A2 XC40 after 2 wiper strokes

As the simulation continued more liquid accumulated around the A-pillar in A2 XC40, while the A1 XC40 remained in a similar state as in Figure 4.15. After almost 3 wiper strokes a significant amount of liquid has accumulated, as seen in Figure 4.16.

Figure 4.16: A2 XC40 after almost 3 wiper strokes

A comparison between A2 XC40 with a wind tunnel test approaching the end of the third wiper stroke, see Figure 4.17, shows a similar accumulation of liquid on the A-pillar. The spreading on the A-pillar differs between A2 XC40 and the wind tunnel test. In the wind tunnel test the liquid is quickly transported across the A-pillar, due to the airflow-liquid interaction, once it crosses the APM whereas the simulation accumulates liquid along the crease between the APM and the A-pillar.

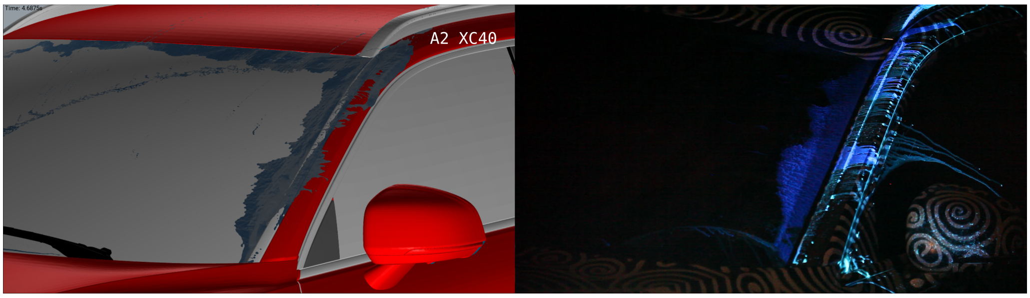

Figure 4.17: A2 XC40 comparison with wind tunnel test at the end of the third wiper stroke

As a way to reduce the accumulation between the APM and the A-pillar the adhesion factor of the APM was reduced to 1, the result can be seen in Figure 4.18.

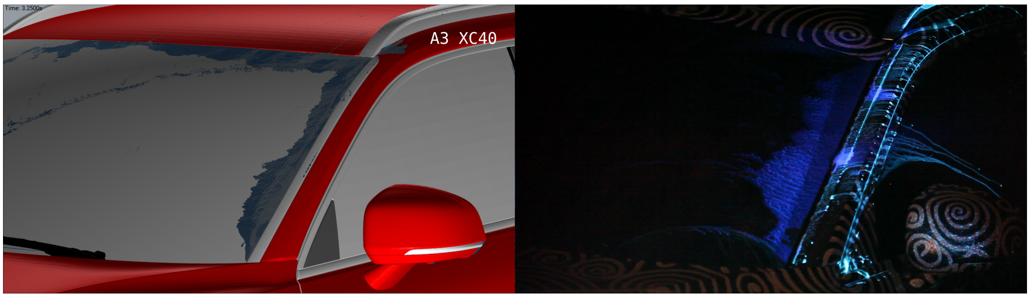

Figure 4.18: A3 XC40 compared with wind tunnel test at the bottom of second wiper stroke

From Figure 4.18 the A-pillar overflow starts at the same three points in both the wind tunnel test and the simulation, but the amount of liquid is significantly different. As the simulation carries on there are significant amounts of liquid accumulating on the A-pillar in A3 XC40 as evident from Figure 4.19.

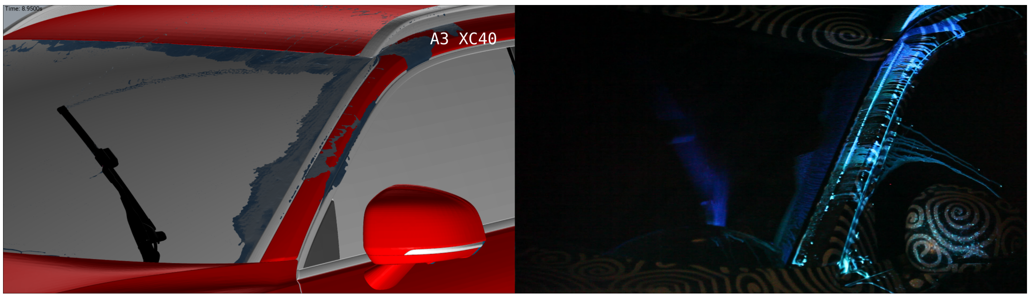

Figure 4.19: A3 XC40 compared with wind tunnel test at the midpoint of the sixth downstroke (t:8.95s)

In A3 XC40 at the midpoint of the sixth downstroke (t=8.95s), Figure 4.19, the liquid accumulates between the A-pillar and the chrome trim. To trigger overflow one could lower the adhesion factor on the chrome trim, applying the same tactics as when the liquid accumulated in the groove between the APM and A-pillar in A2 XC40. The order of hydrophilicity from most hydrophilic to least among the materials used in the A-pillar region are: windshield/chrome trim, painted aluminium/steel and last the APM. The order of hydrophilicity conclusion is supported by Table 4.1, but the table also highlights the large differences in hydrophilicity. When comparing the contact angle of the clear coat assumed to be used on painted aluminium (from in-house measurements) with measurements conducted by another thesis group on painted plastic, using a similar method as described in Section 3.3. Their results showed that the contact angle of painted plastic was about half of that of the clear coat assumed to be used on painted aluminium. If using the values derived from the measurements of the painted plastic it renders the painted aluminium and the APM equally hydrophilic. When using the same adhesion factor on the APM as the A-pillar, see simulation A2 XC40 the liquid accumulated in the crease between the APM and the A-pillar, i.e by manipulating the adhesion of the individual parts one can control where the liquid ends up, further highlighting the importance of correct surface properties.

4.3.2 Influence of liquid properties

The properties used for the static V90 and validation simulations were those of water. Reason being that studies on droplets or water morphology could be found easier. The static windscreen washing test was performed both with water and wiper fluid, in case future simulations would be done using wiper fluid. The properties of water were kept when tuning the simulation model to the physical test with wiper fluid. The first problem with this approach emerged when changing from water to using wiper liquid in the simulations. The change was applied between the A1 V90 and A2 V90 simulations and the aim was to see if the wiper fluid properties made a noticeable difference in the simulations. During the initial pre-wash there was a large difference in pooling around the injector impact points. For a comparison see Figure 4.20.

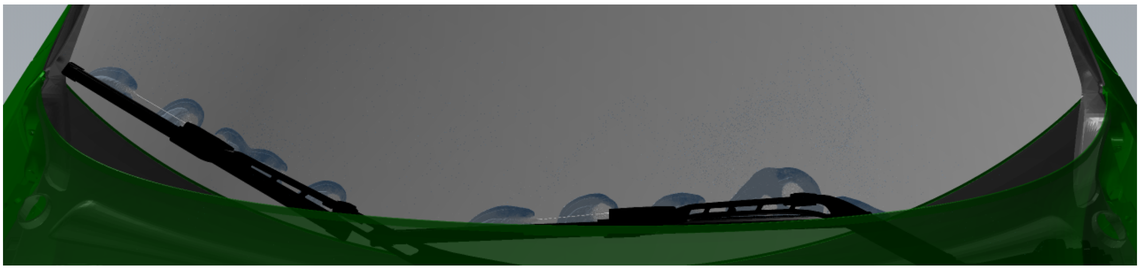

(a) A1 V90, with water, at t:0.3s

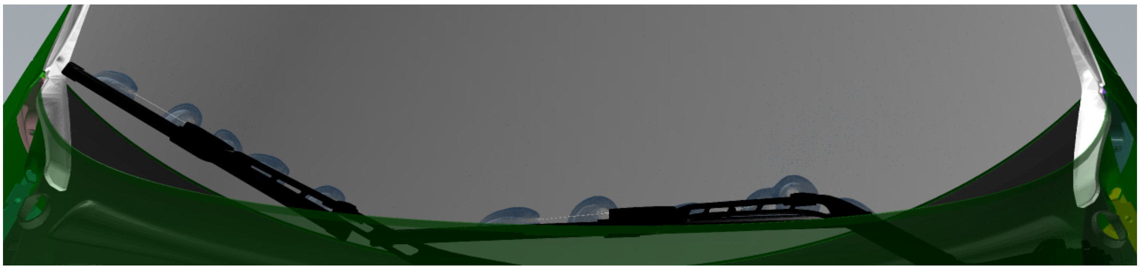

(b) A2 V90, with washing liquid, at t:0.3s

Figure 4.20: Comparison between A1 V90 in the top and A2 V90 in the bottom at t:0.3s

Figure 4.20 shows that A1 V90 has a larger pooling area around the impacting zones of the wiper liquid on the windscreen. The main reason could be the viscosity since the only parameters differing between both simulations are the viscosity and density. It seems unlikely that the density would make a large difference since the density difference is a lot smaller.

For the top position there are also some major differences between the two simulations, see Figure 4.21.

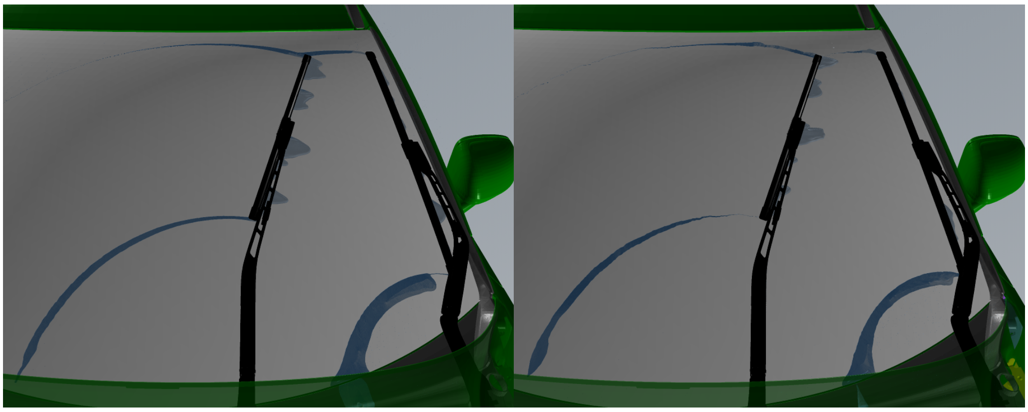

Figure 4.21: A1 V90, with water, to the left and A2 V90, with washing liquid, to the right after the first upstroke

There is a thicker and more evident overspray under the driver side wiper tip in A1 V90 than in A2 V90. The fluid pattern in the area between the passenger and driver side wiper is larger in A1 V90 than in A2 V90. Also this difference is likely to be down to viscosity differences. The momentum of the fluid is the same as the wiper blades are starting to retard as they approach the top wiper position. When this happens there are three mechanisms of action to slow down the fluid: surface properties (adhesion and roughness factor), drag loss from the airflow and viscosity. Since the surface properties and airflow are the same in both simulations and lower viscosity should yield a larger fluid surface area this is the most likely explanation. The fluid behaviour is different for both simulations but neither is correct when compared with the wind tunnel test.

4.3.3 Influence of airflow parameters

The A2 V90 at the beginning of first downstroke is presented in Figure 4.22.

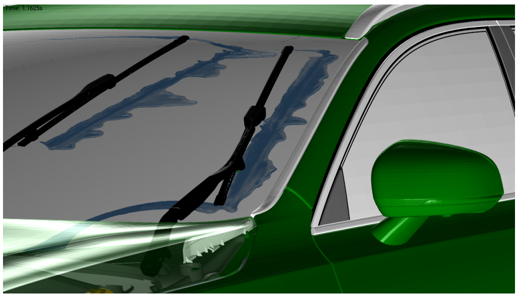

Figure 4.22: A2 V90 at the beginning of first downstroke

In Figure 4.22 the fluid is not affected by the airflow to a large enough degree. Specifically, in the wind tunnel test the fluid is travelling upwards along the A-pillar, but in the simulation A1 V90 the fluid is travelling downwards along A-pillar. A reason for this could be that the airflow and the implementation of the drag equation, see Equation 2.9 into the SPH solver demands that also this parameter is tuned. A motivation for this could be that the mass of a sphere has a cubic dependence on the particle sizing, i.e if the diameter of the particle is doubled the mass is increased by a factor of 8. In contrast the drag equation has a quadratic dependence, i.e if the diameter of the particle is doubled the force is only increased by a factor of 4. This will lead to a skewed ratio between the gravitational force and the airflow forces induced on the particle as the particle size is changed. A scaling factor of 1.5 of the velocity vectors was therefore introduced in A3 V90. The objective was to increase the force acting on the particles from the airflow and as a consequence try to correct the ratio between the gravitational forces and the aerodynamic forces. Since the velocity vectors of the airflow were only scaled the flow structures should be kept, which would not be the case if just using an airflow simulated at a higher velocity. Some results from the simulation can be seen in Figure 4.23.

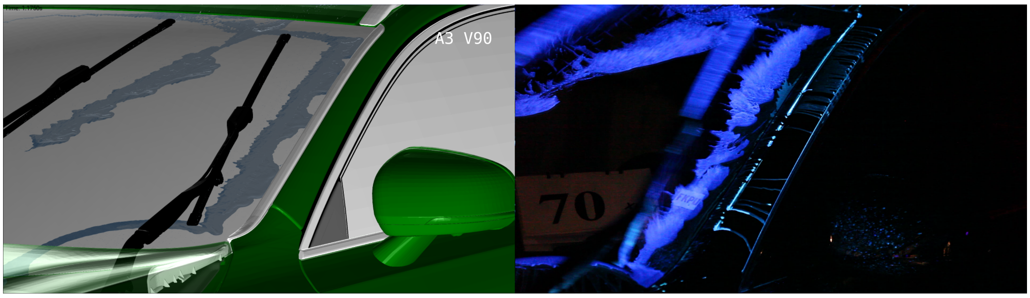

Figure 4.23: Comparison between A3 V90 and wind tunnel test at the beginning of first downstroke

By looking at Figure 4.23 and the area between the passenger and driver side wiper it can be noted that the fluid is moving upward the windscreen in both wind tunnel test and A3 V90. There are also similarities in the distribution, with more fluid being concentrated towards the tip of the wiper. In the region between the A-pillar and the driver side wiper the turbulent behaviour in the wind tunnel test there is a lot of turbulence, most visible in the middle part of the A-pillar where multiple streaks of fluid are going in different directions. Some of the streaks are generated by the pullback effect from the driver side wiper. The pullback from the driver side wiper is believed to be a product of mainly two things, the low pressure wake behind the wiper blade and the force generated on the fluid by the wiper blade pulling away where force is applied through adhesion. Why the behaviour is not properly captured in A3 V90 is unknown, it is clear that the aerodynamic forces on the fluid is captured better by A3 V90 than in A2 V90, see Figure 4.22. However, in Figure 4.23 more force should be transferred from the airflow in the simulation. The force applied on the fluid through the force of adhesion might also play a role, but should have less impact than the aerodynamic forces.

In Figure 4.24 A3 V90 has a larger shearing force acting on the fluid as the fluid is flowing with a higher velocity upward of the windscreen. The shape of the fluid in the area between the passenger and driver side wiper is also different, the A2 V90 has a lot of fluid trajecting in the normal direction of the passenger side wiper. The A3 V90 has fluid flowing along the passenger wiper blade. For the A-pillar region, the shape of the fluid is similar but the A3 V90 has a larger wetting area, as parts of the fluid are in contact with the A-pillar, which is to be expected since it has larger forces acting on it.

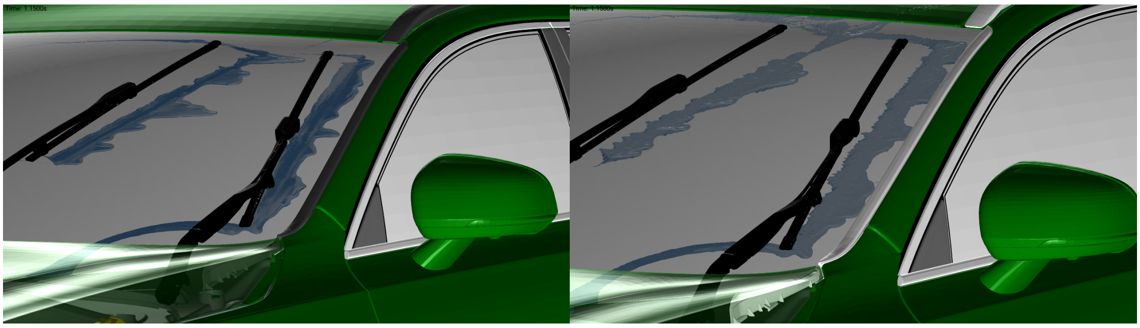

Figure 4.24: A2 V90 and A3 V90 at the start of the first downstroke

Takeaways from Figure 4.24 and Figure 4.23 is that the airflow is better implemented in A3 V90 than in A2 V90, but a higher velocity scaling could be tested to further increase the aerodynamic forces. The pullback effect from the driver side wiper is not captured in either A2 V90 or A3 V90 when compared with the wind tunnel test in Figure 4.23. The lack of a pullback effect in the simulations might be a result of the airflow in A2 V90 exerting a too small force on the particles. In A3 V90 where the velocity is scaled the airflow around the driver side wiper is only modelled by the generic airflows, see Table 3.2, and is therefore unable to capture the pullback effect of the wiper. Pullback effect is not believed to be necessary to model A-pillar overflow correctly, but it is one of the qualitative analysis one can do on the V90 with really low amounts of A-pillar overflow.

The A4 V90 simulation was run to show the need for simpler validation cases. By running settings that are clearly wrong (by changing the gravitational constant) while still getting a better results. Figure 4.25 shows a comparison between A2 V90 with A4 V90.

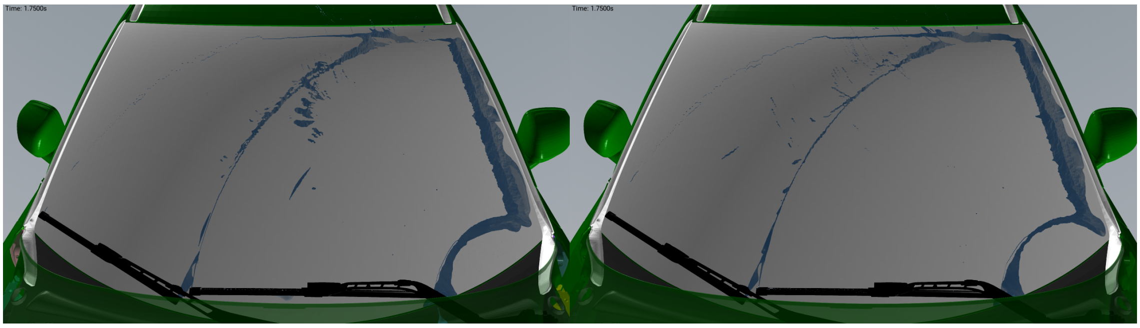

Figure 4.25: A2 V90 (left figure) and A4 V90 (right figure) at bottom reversing position after first wiper cycle.

The decreased gravitational constant causes the fluid to flow upwards along the A-pillar, which makes this simulation more realistic than A2 V90.

A5 V90 with the scaled velocity vectors at the beginning of the first downstroke is shown in Figure 4.26 from two perspectives.

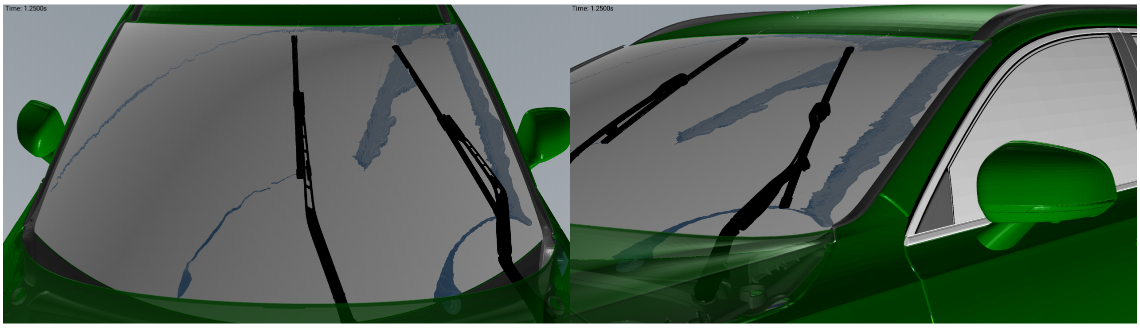

Figure 4.26: A5 V90 from two perspectives at the beginning of the first downstroke

The increased scaling of the velocity vectors causes the liquid to flow upwards along the A-pillar, in almost the same manner as in A4 V90. In this case, since the A4 V90 has the wrong gravitational constant, it is verified that it is wrong. If it is not obvious as to what is right, the method applied makes it easy to go in a wrong direction or hitting a local maxima in terms of accuracy.

In the V90 simulations with airflow implemented the tuning parameter used was the scaling of the velocity vectors. This approach required CFD software to be used in order to apply the change, since it's not time-efficient and not always possible to do this operation another approach using the density as a tuning parameter was tested. This is not strictly comparable as at least two factors in the drag model used are believed to be non-linear where as the density scaling is linear. The velocity scaling is quadratic and the behavior of the variable C_d value is not available. The velocity of the the airflow is also different between the two simulation models, which is why a fair comparison between the two PreonLab models cannot be done. By comparing the relative difference between the V90 Preonlab model and its wind tunnel test and the XC40 PreonLab model and its wind tunnel test, the influence of the density and velocity scaling can be compared.

In comparison with A3 V90, where the velocity was scaled by a factor of 1.5, A1 XC40 utilised a density scaled by a factor of 2.25. In Figure 4.27 A1 XC40 at the top wiper position in the first wiper stroke is compared to a wind tunnel test.

Figure 4.27: A1 XC40 and wind tunnel test at top wiper position in the first wiper stroke

Figure 4.27 highlights that there are problems with capturing the spreading around both of the wiper blades in the simulations. The spreading around the PS wiper blade shows that liquid is kept closer to the wiper blade when compared to the wind tunnel test. Reasons could still be adhesion factor, roughness factor and airflow density scaling. However, the airflow implementation is severely lacking, as shown in Figure 4.28-4.29 where the liquid adhesion to the wiper blade seems to be the main force behind the pullback in the A1 XC40 simulation.

Figure 4.28: A1 XC40 and wind tunnel after hitting top wiper position in the first wiper stroke

Figure 4.29: A1 XC40 and wind tunnel at the start of first downstroke

The Figures 4.28-4.29 shows that the pullback effect in the simulation is evident as long as the wiper blade stays in contact. In the wind tunnel test it is obvious that the pullback effect stems mainly from the low pressure in the wake of the DS wiper blade as the liquid starts to detach from the DS wiper blade in Figure 4.28 while the pullback effect is in effect even in Figure 4.29.

4.3.4 Comparison of V90 and XC40

The Volvo V90 and XC40 are very different in the amount of A-pillar overflow and the Figures 4.30a-4.30b show different time steps from wind tunnel tests.

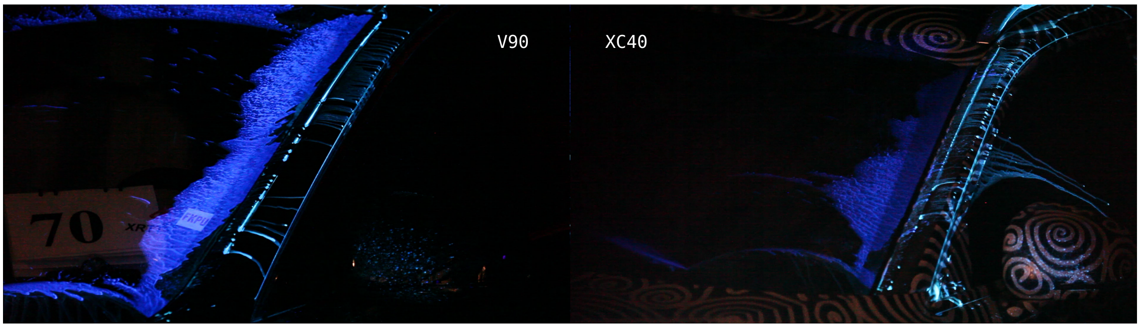

(a) V90 and XC40 after the first downstroke

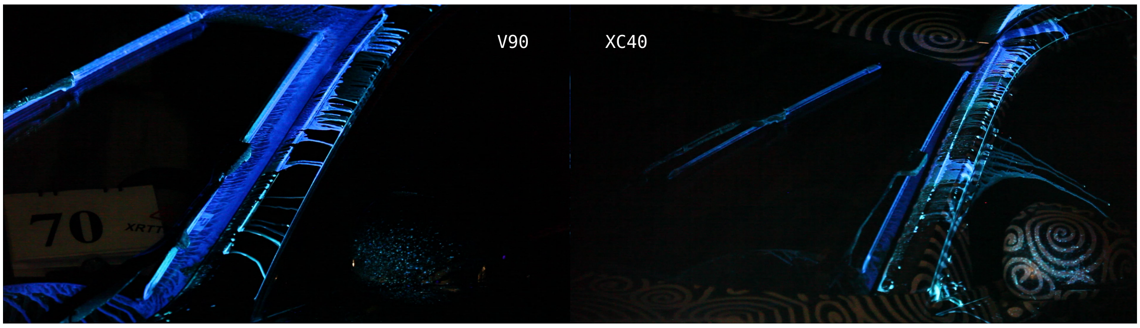

(b) V90 and XC40 at the top of the fifth wiper stroke

Note that the overflow of interest is primarily the A-pillar overflow that ends up on the driver side window. From the Figures 4.30a-4.30b it does not look as if there is an obvious difference between the two vehicle models.

In Figure 4.31 the V90 and the XC40 at a later stage in the wind tunnel tests are compared and the difference in overflow is clear.

Figure 4.31: V90 and XC40 at a late stage in wind tunnel tests

The last simulation on the V90, A6 V90, was run according to the settings used in simulation A3 XC40. A6 V90 is compared to a wind tunnel test at the start of the third downstroke in Figure 4.32

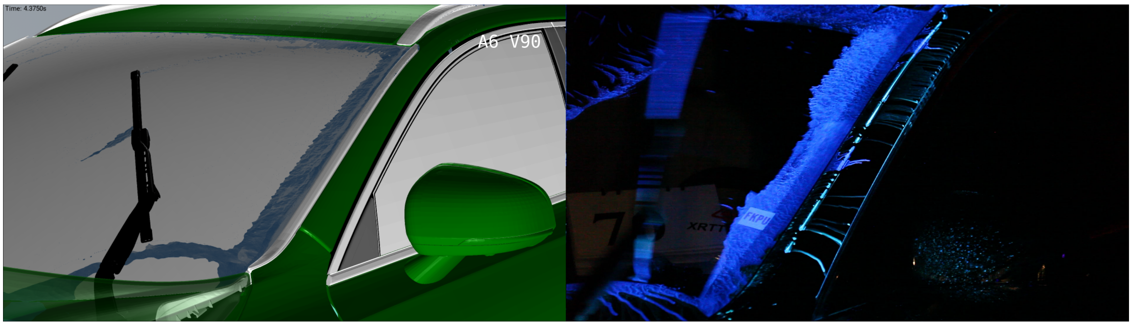

Figure 4.32: A6 V90 compared with wind tunnel test at t:4.375s

The implementation of the surface properties used in A3 XC40 did not alter the A-pillar overflow, which is still non-existent in the simulation. The small impact is expected since the only change between A6 V90 and A5 V90 is the surface properties of the APM. A6 V90 shows that more tuning on the airflow-liquid model is needed.

A comparison between the A6 V90 and A3 XC40 at the top of the third wiper stroke can be seen in Figure 4.33.

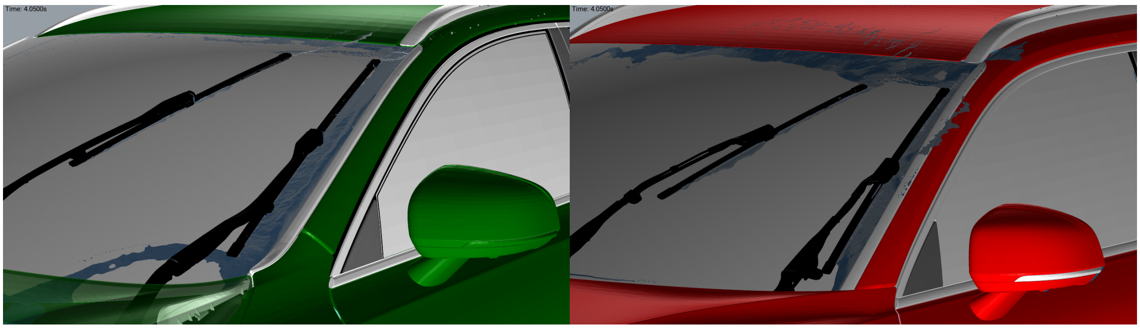

Figure 4.33: A6 V90 and A3 XC40

Figure 4.33 shows a complete lack of A-pillar overflow in A6 V90 while the A3 XC40 has started producing some. The main differences between the two simulation models are the geometry, injection scheme and airflow-liquid interaction. The differences in wind tunnel tests start to differ between the two vehicle models at a late stage but were similar up to the point when the overflow reached the driver side window. The two simulations, A6 V90 and A3 XC40, deviate more than their wind tunnel test counterparts. The reason is not clear as the higher velocity used in the A3 XC40 could contribute to a larger extent than the lower velocity used in the A6 V90. The different injection schemes between A6 V90 and A3 XC40 could also be an explanation.

4.3.5 Reflections on results gained in the thesis

This thesis ends with a set of questions unanswered, primarily about particle size, surface properties and airflow-liquid interaction. The tuning of surface properties has proven to be a time-consuming task and A-pillar overflow simulations are not a suitable way of retrieving the surface properties due to the computational cost and the number of uncertainties. Previous work in the Contamination & Core CFD Department has been done on vehicle wading using PreonLab. The work stems from the thesis work of Johan Idoffsson and shows that when surface properties are of low importance PreonLab works well [9]. When tuning the surface properties for glass and water, see Section 4.2, the Pairwise-Force model employed showed good results when using a fine particle spacing, see Figure 4.6, and slightly worse when compared with a coarser particle spacing. The fine particle size was 0.0625mm and is almost half of the particle size used in the A-pillar overflow simulations. Several possible explanations as to why the results from the impacting droplet study did not carry over to the A-pillar overflow simulation exist. As capturing the correct contact angles both statically and dynamically is a study in itself with its own limitations, the suggestion is to tune the surface properties according to what one is interested in. If the interesting case is impacting droplets on a glass surface use Section 3.4 or if it is capturing static contact angles see Section 3.3. A suggestion for future studies is the testing of smaller quantities of liquid, with different particle sizing, flowing on plates of different materials and tuning the adhesion and roughness factor to the tests. With the use of specific tests the uncertainties of advancing and receding contact angles, to name a few, will not have to be dealt with, as the contact angle itself might be the result of other causes. An example is the use of a too coarse particle size, where the induced contact angle for a liquid film might be zero degrees (one layer of particle thick) and it could still be tuned to have a decent spreading rate and behaviour. The hypothesis is that as long as the Pairwise Force model in PreonLab is not validated with different particle sizing the surface properties derived should be the result of very specific, yet simple, tests.

The airflow-liquid interaction has not been fully investigated as the number of different airflow setups were few and with the uncertainties from the surface properties it is difficult to make a qualitative judgement from the different setups used. Future studies should be done on which surface-liquid model to use, and how to deal with the difference in particle sizing. The previously suggested test of liquid flowing on a plate at varying angles could be expanded to also tune the airflow-liquid model.

The particle size was set based on the maximum memory available on the cluster nodes used, leaving the particle sizing convergence test unanswered. In order to test the particle sizing a different test case should be used since the A-pillar overflow simulations are computationally costly, but since the limitation is the hardware used the real question is if the chosen particle size of 0.125mm is small enough to capture the relevant physics. The particle size used will directly affect surface properties and airflow-liquid interaction. Why the particle size affects the liquid-surface behaviour is believed to be a change in force balance for a particle. How it changes is unclear, but what is known is that the mass of a particle will increase by a factor of 8 if the particle size is doubled. The gravitational force exerted on a liquid particle will therefore increase dramatically. To keep the force balance the surface tension forces for a particle will have to increase equally. The same principle can be applied on the airflow-liquid interaction as the projected area, A_p, will not increase at the same rate as the mass of the particle and result in different particle sizes needing different density, or vector, scaling for the airflow to counteract the shift in force balance.

A recent PreonLab version can use continuous particle sizing which opens up new possibilities both in terms of accuracy of the simulations and the computational cost. The updated version was introduced at a late stage of the thesis and the use of continuous particle sizing was not investigated. The version does not support continuous model parameters, and the lack of a varying adhesion factor, roughness factor and density/vector scaling for the airflow-liquid model would likely induce accuracy problems as it would skew the force balance of the particles. If continuous model parameters were to be implemented in the future it could decrease the computational cost and at the same time capture A-pillar overflow more accurate.

The workflow used to build the simulation environment in the thesis can be used, but changes to the windscreen or wiper blade geometry are time consuming and should be avoided. An estimate of the time required to build a new simulation environment with a new vehicle model is approximately two weeks. After the initial simulation setup is built the vehicle geometry, wiper cycle, surface properties can be changed within minutes or within a few hours depending on what changes need to be applied. A part of the purpose was to derive a workflow to aid in early design changes, but changes to wiper or windscreen geometry makes the workflow slow and would not be suitable before windscreen and wiper geometry is set. The simulations are computationally heavy and with a cluster time of closer to two weeks needed to reach overflow in the current status it makes it hard to motivate the use today.

5
Conclusion

It is possible to model a transient windscreen washing event with a complete wiper system using PreonLab and ADAMS. However, the results from the simulations are not satisfactory in terms of capturing A-pillar overflow and further work needs to be carried out to achieve good results. The main area of improvement is tuning the model parameters for surface-liquid and airflow-liquid interaction. The workflow used to build the simulation environment in the thesis can be used, but changes to the windscreen or wiper blade geometry are time consuming and should be avoided. After the initial simulation setup is built most simulation geometries or settings can be changed quickly. The simulations are computationally costly, thus making it hard to motivate the use today.

In the future, if continuous particle sizing were to be tested and better validation cases could be used for tuning the model parameters discussed (adhesion factor, roughness factor and airflow-liquid interaction), it might be a different case. The computational cost could be decreased with continuous particle sizing and the force balance for the particles could be kept with continuous model parameters. Therefore, the recommended future work is the development of easier validation tests for tuning model parameters and testing continuous particle sizing. If a continuous model parameter is not implemented in the SPH-solver the use of continuous particle sizing will not be beneficial as the force balance for a particle will alter with the particle size.

By solving the problems with surface-liquid and airflow-liquid interaction an SPH-based solver might be a viable alternative to FVM-based solvers as the need for remeshing due to topology change is removed. A suitable way of deriving these parameters needs to be investigated and a way of how to do so has been suggested. A benefit that the thesis has shown is that the interaction between PreonLab and ADAMS works well and that a similar workflow could be utilized for other applications. The problem with the A-pillar overflow simulations does not lie directly with the use of an SPH solver, but more with the fact that FVM-based solvers have been tuned and are validated to a larger extent. There is also a lack of validation when it comes to using SPH for capturing surface-liquid interaction in general.

Bibliography

[1] J. J. Monaghan, "Smoothed particle hydrodynamics," *Annual Review of Astronomy and Astrophysics*, vol. 30, no. 1, pp. 543–574, Sep. 1992. DOI: 10.1146/annurev.aa.30.090192.002551. [Online]. Available: https://doi.org/10.1146/annurev.aa.30.090192.002551.

[2] ——, "Smoothed particle hydrodynamics," *Reports on Progress in Physics*, vol. 68, no. 8, pp. 1703–1759, Jul. 2005. DOI: 10.1088/0034-4885/68/8/r01. [Online]. Available: https://doi.org/10.1088/0034-4885/68/8/r01.

[3] ——, "Smoothed particle hydrodynamics and its diverse applications," *Annual Review of Fluid Mechanics*, vol. 44, no. 1, pp. 323–346, Jan. 2012. DOI: 10.1146/annurev-fluid-120710-101220. [Online]. Available: https://doi.org/10.1146/annurev-fluid-120710-101220.

[4] Z.-B. Wang, R. Chen, H. Wang, Q. Liao, X. Zhu, and S.-Z. Li, "An overview of smoothed particle hydrodynamics for simulating multiphase flow," *Applied Mathematical Modelling*, vol. 40, no. 23-24, pp. 9625–9655, Dec. 2016. DOI: 10.1016/j.apm.2016.06.030. [Online]. Available: https://doi.org/10.1016/j.apm.2016.06.030.

[5] A. B. Liu, D. Mather, and R. D. Reitz, "Modeling the effects of drop drag and breakup on fuel sprays," in *SAE Technical Paper Series*, SAE International, Mar. 1993. DOI: 10.4271/930072. [Online]. Available: https://doi.org/10.4271/930072.

[6] *Intermolecular and Surface Forces*. Elsevier, 2011. DOI: 10.1016/c2009-0-21560-1. [Online]. Available: https://doi.org/10.1016/c2009-0-21560-1.

[7] M. Ihmsen, J. Cornelis, B. Solenthaler, C. Horvath, and M. Teschner, "Implicit incompressible SPH," *IEEE Transactions on Visualization and Computer Graphics*, vol. 20, no. 3, pp. 426–435, Mar. 2014. DOI: 10.1109/tvcg.2013.105. [Online]. Available: https://doi.org/10.1109/tvcg.2013.105.

[8] M. Jiang and B. Zhou, "Droplet behaviors on inclined surfaces with dynamic contact angle," *International Journal of Hydrogen Energy*, vol. 45, no. 54, pp. 29 848–29 860, Nov. 2020. DOI: 10.1016/j.ijhydene.2019.07.173. [Online]. Available: https://doi.org/10.1016/j.ijhydene.2019.07.173.

[9] J. Idoffsson, "Wading – evaluation of sph-based simulations versus traditional finite volume cfd," 2019. [Online]. Available: https://hdl.handle.net/20.500.12380/300473.

A

Appendix 1

In Table A.1 the time-steps can be converted to the unit-less time, t^*, as used in Section 3.4

Table A.1: Conversion table for t^* and t

t*	t [s]
0.21943396	0.0005
0.438868	0.001
0.658302	0.0015
0.877736	0.002
1.3166	0.003
1.75547	0.004
2.19434	0.005
2.63321	0.006
3.07208	0.007
3.51094	0.008
3.94981	0.009
5.26642	0.012
7.02189	0.016
8.77736	0.02

A.1 Computational Statistics

Statistics of RAM usage, time step, number of particles simulated, number of solid particles simulated from the simulation A4 V90 is presented in Figure A.1, A.2, A.3 and A.4 respectively.

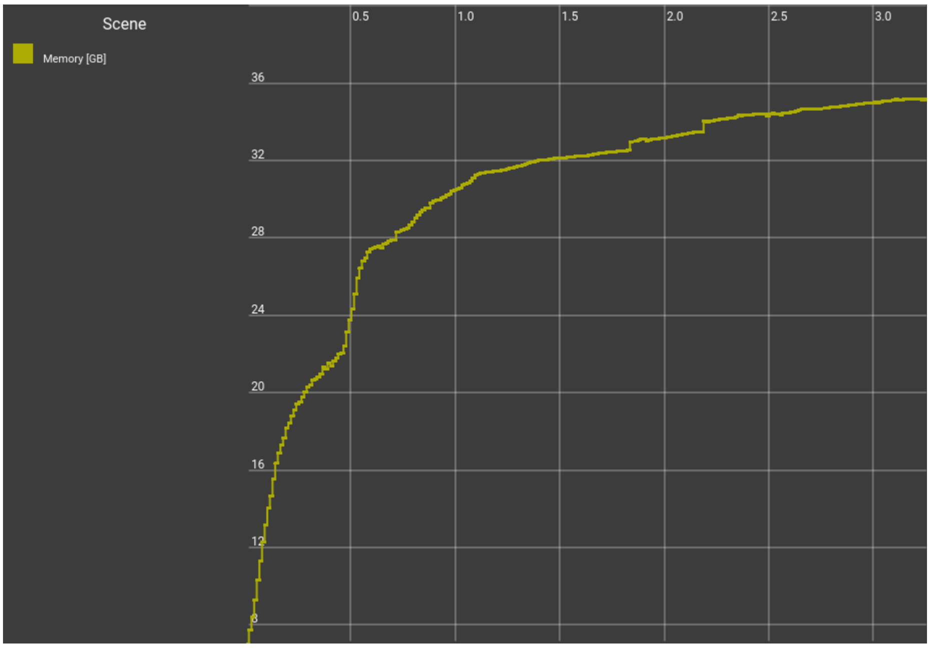

Figure A.1: RAM usage [GB] against simulated time [s]

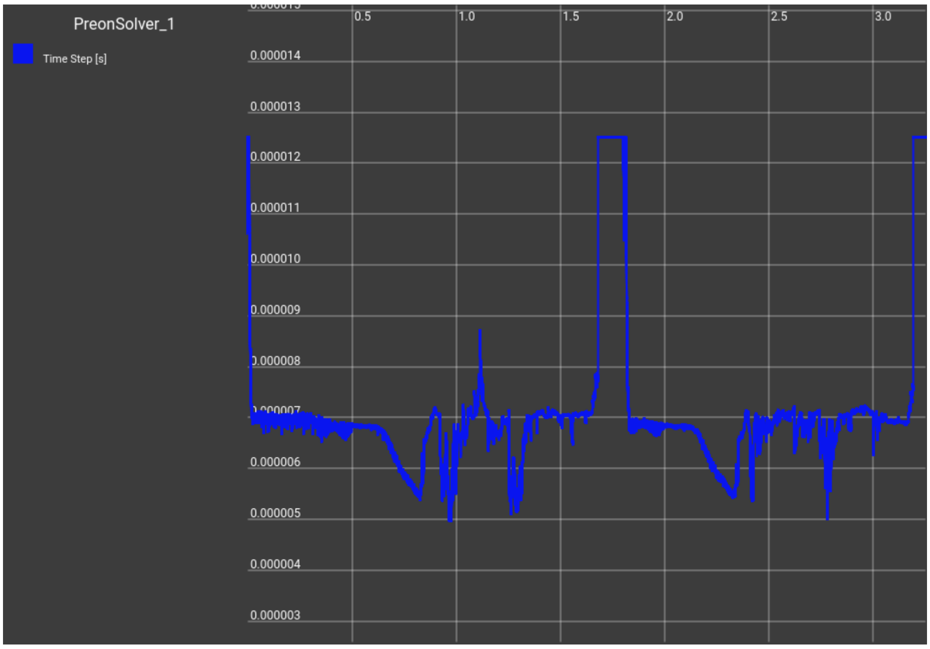

Figure A.2: time step [s] against simulated time [s]

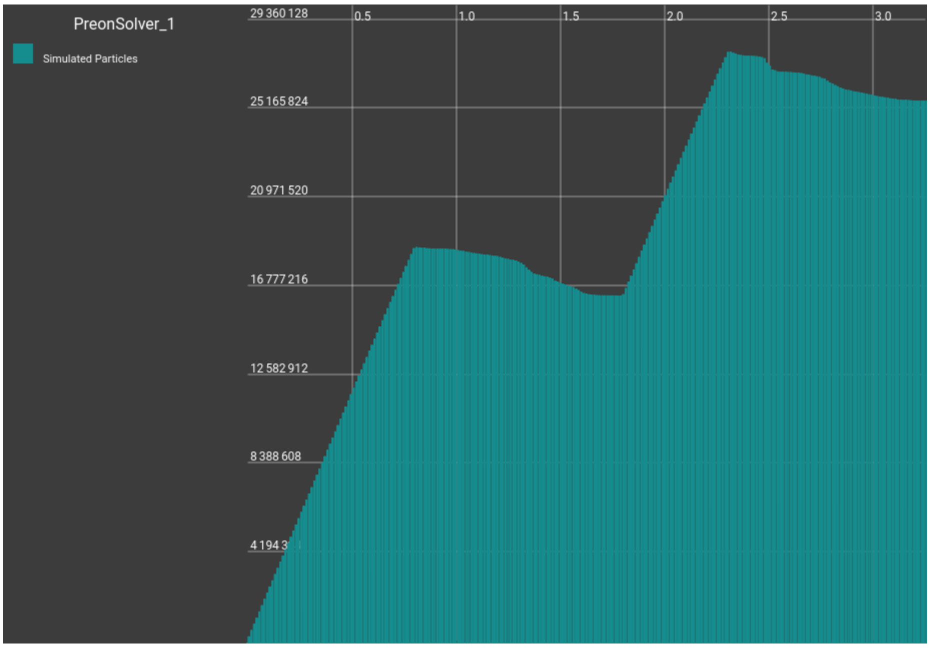

Figure A.3: Number of fluid particles modelled against simulated time [s]

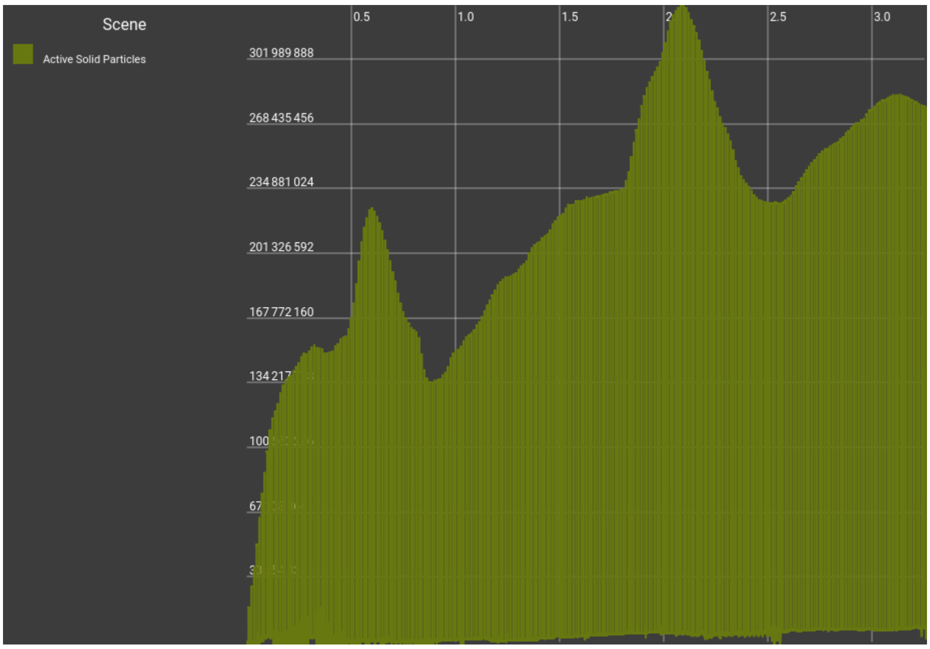

Figure A.4: Number of solid particles modelled against time [s]

Statistics of RAM usage, time step, number of particles simulated, number of solid particles simulated from the simulation A2 XC40 is presented in Figure A.5, A.6, A.7 and A.8 respecitvely.

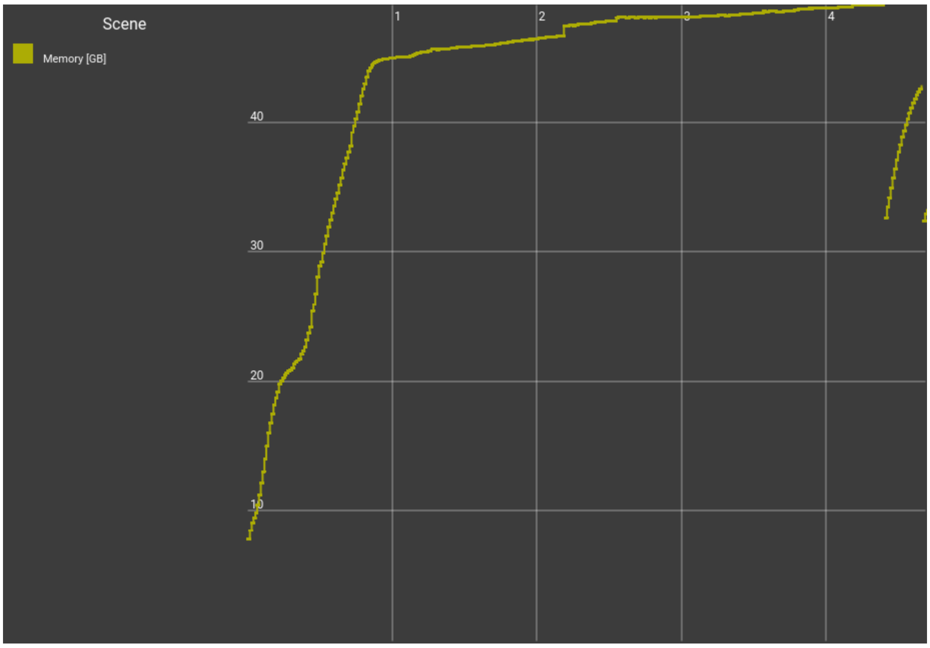

Figure A.5: RAM usage [GB] against simulated time [s]

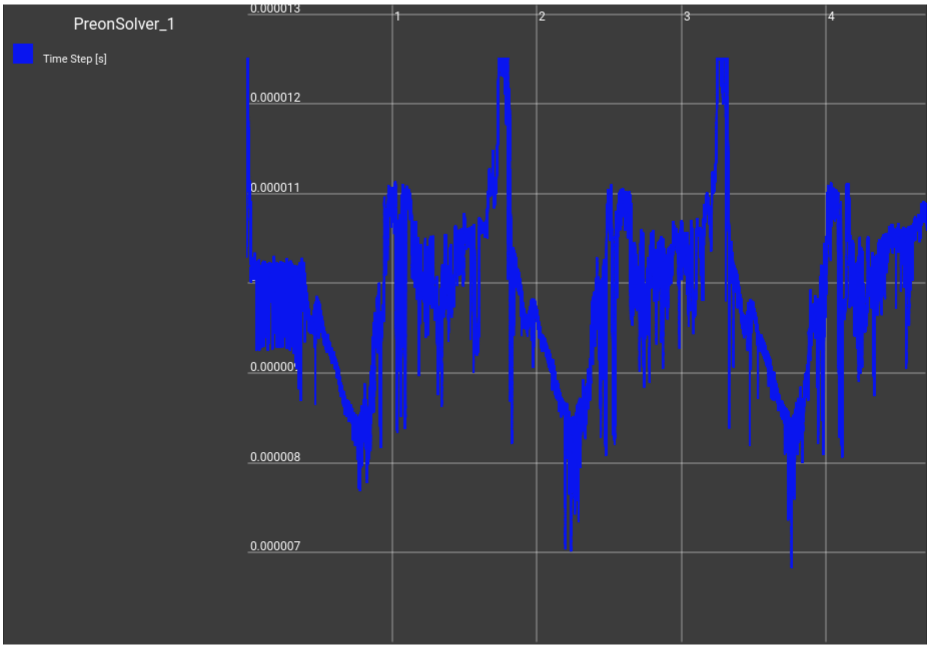

Figure A.6: time step [s] against simulated time [s]

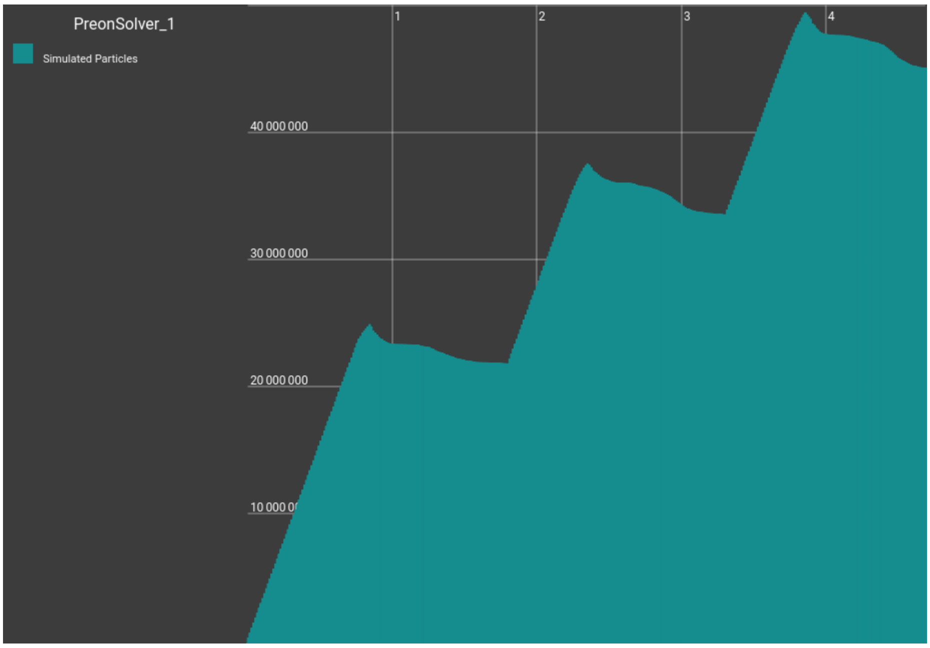

Figure A.7: Number of fluid particles modelled against simulated time [s]

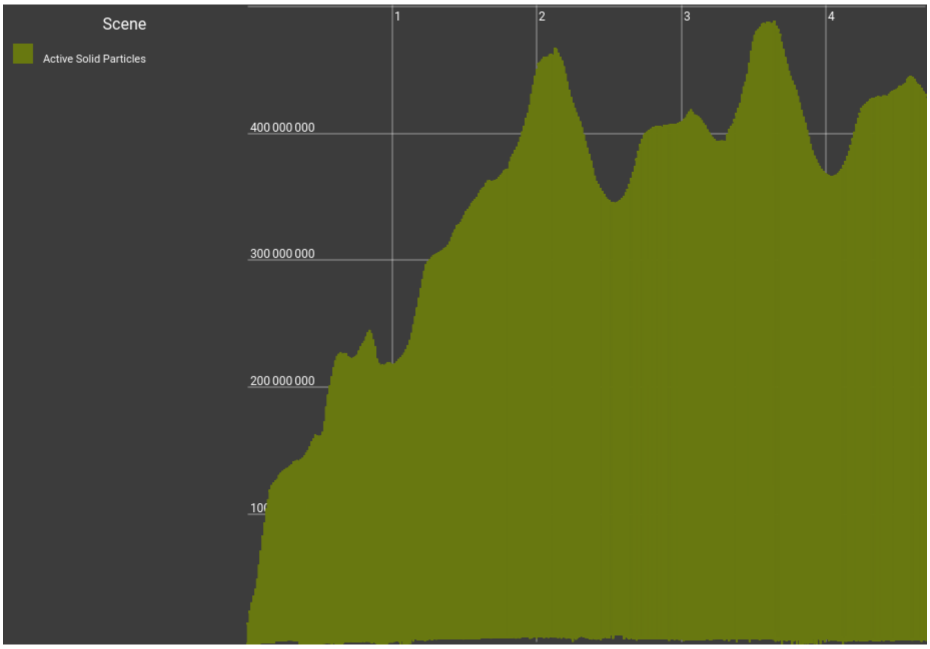

Figure A.8: Number of solid particles modelled against time [s]